Check for updates

Radio Science

RESEARCH ARTICLE
10.1029/2021RS007299

Ocean Surface Radial Velocity Imaging in the AT-INSAR Velocity Bunching Model: A Functional Approach

Fabricio Pérez[1,2], **Miguel Angel Moreles**[1], **and J. Héctor Morales-Barcenas**[3]

[1]Centro de Investigación en Matemáticas (CIMAT), Guanajuato, México, [2]Mathematics Department, Universidad de Guadalajara, CUCEI, Guadalajara, Mexico, [3]Departamento de Matemáticas, Universidad Autónoma Metropolitana - Iztapalapa, Ciudad de Mexico, México

Key Points:

- The scalar field of radial velocities of a simulated ocean surface is constructed from a noisy along-track interferometric synthetic aperture radar (AT-INSAR) image of that surface
- The nonlinear integral equation that relates radial velocities to AT-INSAR intensities is solved by Newton's methods on function spaces
- Robustness is illustrated by recovering fields of radial velocities for different R/V ratios and other radar parameters

Correspondence to:
M. A. Moreles,
moreles@cimat.mx

Citation:
Pérez, F., Moreles, M. A., & Morales-Barcenas, J. H. (2021). Ocean surface radial velocity imaging in the AT-INSAR velocity bunching model: A functional approach. *Radio Science*, *56*, e2021RS007299. https://doi.org/10.1029/2021RS007299

Received 21 APR 2021
Accepted 26 OCT 2021

Author Contributions:
Conceptualization: Miguel Angel Moreles, J. Héctor Morales-Barcenas
Data curation: Fabricio Pérez, J. Héctor Morales-Barcenas
Formal analysis: Miguel Angel Moreles, J. Héctor Morales-Barcenas
Investigation: Fabricio Pérez, Miguel Angel Moreles, J. Héctor Morales-Barcenas
Methodology: Fabricio Pérez, Miguel Angel Moreles, J. Héctor Morales-Barcenas
Software: Fabricio Pérez
Supervision: Miguel Angel Moreles
Validation: Fabricio Pérez
Visualization: Fabricio Pérez

© 2021 The Authors.
This is an open access article under the terms of the Creative Commons Attribution-NonCommercial License, which permits use, distribution and reproduction in any medium, provided the original work is properly cited and is not used for commercial purposes.

Abstract Images obtained by airborne along-track interferometric synthetic aperture radar (AT-INSAR), provide tools to obtain ocean surface properties, such as the radial velocities of sea surface elevations. The estimation of these radial velocities from AT-INSAR images is the interest of this work. We assume the Velocity Bunching Model relating the complex AT-INSAR image at a point in the image plane, with the radial velocity of a scatterer point in the sea surface. The relation is by means of a nonlinear integral operator. Consequently, the estimation of radial velocities amounts to the solution of nonlinear and oscillatory integral equations. Our proposal is to solve the latter by Newton's methods on Hilbert function spaces, the so-called optimize then discretize approach. The effectiveness is illustrated by means of numerical simulations evaluating the reconstruction of the radial velocities and the AT-INSAR image. We show that this continuous version is accurate, and faster than the classical discretize then optimize version. A physical comparison is also carried out with the interferometric velocities.

1. Introduction

In recent decades, imaging of the surface of our planet Earth has increased with the appearance and improvement of tele-detection systems, such as Synthetic Aperture Radar (SAR). A SAR system is capable of constructing an image from the information of electromagnetic waves, which are firstly emitted by the radar and then backscattered by the observed region. See Moreira et al. (2013) for a basic introduction on the subject.

Within the oceanographical context, radar engineers have found that SAR imaging can be successfully applied to measure ocean surface properties, such as currents or wave energy, for example. This adds to the well-known fact that a particular sea state can be statistically modeled by an appropriate two-dimensional directional wave spectrum (Holthuijsen, 2007).

Consequently, an ongoing research problem consists of finding the relationship between SAR images and ocean wave spectra. The literature on this subject is vast. For starters, see the work of Alpers (1983), where such relationship is studied. Therein, it is shown that the SAR response to the moving ocean wavefield is a nonlinear process for a large range of ocean wave parameters. This means that, in order to determine an ocean wave spectrum, a nonlinear inverse problem is to be solved.

In K. Hasselmann and Hasselmann (1991), a mapping of an ocean wave spectrum into a SAR image spectrum is given by a closed integral transform. It is noted that the problem is undetermined when trying to solve for the wave spectrum, and a unique formal inversion of the forward mapping relation cannot exist. The classical approach is to solve a regularized least squares problem, where the cost function is the squared norm of the observed fitted SAR spectra plus a regularization term that uses additional information from a first-guess wave spectrum. The numerical solution is based a quasi-Newton method scheme. This algorithm is improved in S. Hasselmann et al. (1996), by introducing a modified cost function with an additional iteration loop, such that the first-guess input spectrum is systematically updated.

In the aforementioned works, the observed nonlinear relationship between ocean wave spectra and SAR image spectra stress the effect of *velocity bunching*. This term is used to describe variations on the *scatter density* due to a fluctuating *surface radial velocity*. This physical mechanism causes the formation of wave-like patterns on SAR images of the ocean surface. For more details, see Alpers and Rufenach (1979) and K. Hasselmann et al. (1985).

Writing – original draft: Fabricio Pérez, Miguel Angel Moreles, J. Héctor Morales-Barcenas
Writing – review & editing: Fabricio Pérez, Miguel Angel Moreles, J. Héctor Morales-Barcenas

The retrieval of the field of radial velocities is a problem that has attracted some attention recently. It provides complementary information to existing ocean observation systems, see Hwang et al. (2013) and Moiseev et al. (2020). In the former, for instance, the interferometric velocity is used to observe wave breaking in swell-dominant conditions, and its own references provide further motivation on the imaging problem that is developed below.

Goldstein and Zebker (1987) proposed the so-called airborne along-track interferometric synthetic aperture radar (AT-INSAR). Under this scheme, the radar data is acquired by two antennas, the fore and the aft, which are carried (in baseline) by a flying platform in the along-track direction at a given speed. While the aft antenna transmits the signals, both antennas receive the backscattered signals. Each antenna generates its own raw data, which is processed to produce its corresponding SAR image. After this, both SAR images are combined interferometrically to get the AT-INSAR image. A well-known fact is that the phase difference that is caused by the motion of the surface is proportional to the interferometric velocity. Thus, when the velocity bunching mechanism is a linear process, the interferometric velocity is an appropriate approximation to the surface radial velocity in the wave parameter range. The characterization of this parameter range is presented in Alpers et al. (1981) and Alpers and Rufenach (1979).

Unlike (Goldstein & Zebker, 1987), the purpose of the present work is to retrieve the scalar field of radial velocities when the velocity bunching mechanism is a nonlinear process. Our model of reference is the AT-INSAR Velocity Bunching Model presented in Bao et al. (1997). Such a model relates the complex AT-INSAR image at a point in the image plane, to the radial velocity of a scatterer point in the sea surface. In the mathematical jargon, this relation is given by an integral operator that maps radial velocities into AT-INSAR intensities. Assuming that the radial velocity is known in advance, the AT-INSAR image is readily obtained by quadrature. This is the so-called direct problem. For this work, we consider the following inverse (imaging) problem:

> Given a noisy AT-INSAR image of an unknown scalar field of sea surface elevations, estimate the scalar field of radial velocities that is associated with such surface elevations.

Under the first-study assumption that the ocean surface exhibits a swell sea state, we estimate radial velocities by solving the AT-INSAR velocity bunching integral equation.

The core of the paper is the development of numerical methods for solving the underlying integral equation. It will become apparent that the latter is nonlinear and oscillatory, which makes the solution challenging. Our work may be regarded as a numerical simulation study in line with Estatico et al. (2015) and Yoshida (2016). In the former, the contribution of bunching to show a wavelike pattern of an azimuthal wave by numerical simulation is explored. In the latter, an algorithm is proposed for a buried object detection problem. Such algorithm is based on a regularizing approach in L^p Banach spaces. In our inverse problem, we follow this function space formalism, using the Hilbert properties of L^2. Our motivation is to postpone discretization *until the last moment*, that is, the optimize then discretize approach. It is proven to be more efficient, (Stuart, 2010), and sometimes necessary, (Zuazua, 2005).

The outline is as follows. In Section 2 we recall the AT-INSAR scheme, as well as the AT-INSAR Velocity Bunching Model. Then we develop two modified Newton's methods on function spaces for solution. First a nonlinear system, second as a nonlinear least squares problem. Derivatives are computed in the sense of Fréchet. See for instance Cheney (2001), for the required Functional Analysis.

We work with synthetic data. In Section 3 we generate a field of surface elevations following the classical variance spectra to surfaces approach. We obtain a random 2-D realization of a sea surface. Following Mobley (2016), we develop our own implementation.

In Section 4 we present numerical results for the range traveling waves (RTW) configuration. Satisfactory recovery of the radial velocity field and the ATI-INSAR image is illustrated. The solutions obtained from the nonlinear system and the nonlinear least squares problems are mutually cross-validating. For comparison we implement also a discretize then optimize approach, in the case of minimization. It is shown that as expected, the former perform better and are considerably faster in terms of execution time. A physical comparison is also carried out between the bulk kinetic energy on the ocean surface area under study, associated to the estimated field of radial

velocities and that of the interferometric velocities. The comparison is in terms of relative errors, again, the latter is outperformed.

Some technical information on software and hardware is given in Section 5, followed by conclusions in Section 6.

In Appendix A, additional RTW scenarios are presented as well as scenarios in the azimuthally traveling waves (ATW) configuration. The purpose is to illustrate further the performance of our methodology to recover the radial velocity field, when of the velocity bunching mechanism is a nonlinear process.

2. Materials and Methods

In this section we formulate the imaging problem of interest and we develop the modified Newton's methods for its solution. We follow a functional approach, that is, we optimize on spaces of functions. More precisely, for an interval $(a, b) \subseteq \mathbb{R}$, we consider the normed vector space of square integrable complex functions, denoted as $L^2((a, b))$. This is a Hilbert space equipped with the usual inner product. That is, for any pair of functions ϕ, $\psi \in L^2((a, b))$, the inner product is defined as

$$\langle \phi , \psi \rangle \;=\; \int_a^b \phi(x)\,\overline{\psi(x)}\,dx$$

where $\overline{\psi(x)}$ is the complex conjugate of $\psi(x)$.

We shall freely use all the well-known Hilbertian properties of L^2. These methods of applied analysis are fully covered in Cheney (2001). An attractive feature of this book is the carefully chosen numerical examples. See, for instance, the discussion on Newton's method.

Let us start by recalling the AT-INSAR scheme, as well as the AT-INSAR Velocity Bunching Model.

2.1. The AT-INSAR Scheme

The AT-INSAR scheme given here is based on Bamler and Hartl (1998). The AT-INSAR image is acquired by two separated antennas, the fore and the aft, which are carried (in baseline) by a flying platform in the along-track direction. We assume that the system operates in the so-called mode 1, namely, the aft antenna transmits radar signals, and both antennas receive the backscattered signals. Figure 1 shows the AT-INSAR geometry.

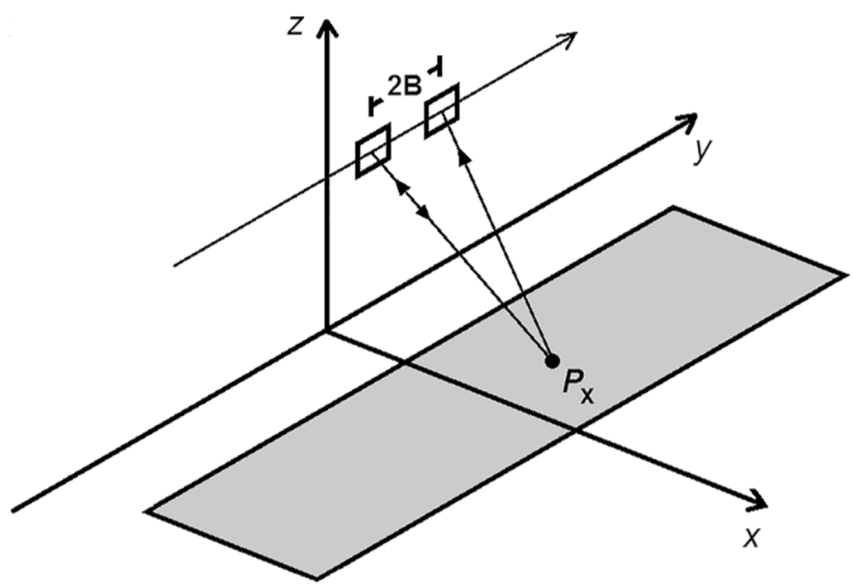

Figure 1. The along-track interferometric synthetic aperture radar geometry.

The following notation is used

- Let x and x_R denote the coordinates in the ground range direction (cross-track).
- Let y and y_R denote the coordinates in the azimuth direction (along-track).
- Let $\mathbf{x} = (x, y)$ denote a point in the reference frame of the sea surface.
- Let $\mathbf{x}_R = (x_R, y_R)$ denote a point in the AT-INSAR image plane.
- Let $P_{\mathbf{x}}$ denote the scatterer at the point $(\mathbf{x}, z(\mathbf{x}))$.
- Let B denote half the separation between the antennas.
- Let V denote the constant speed of the flying platform.
- Let R denote the distance from the median of the two antennas to $P_{\mathbf{x}}$.

The acquired AT-INSAR image at the position $\mathbf{x}_R$ that is associated with $P_{\mathbf{x}}$, is the complex function $I(\mathbf{x}_R)$.

For each point $\mathbf{x} = (x, y)$ in the reference frame of the sea surface (Figure 1), there is a corresponding unique point $\mathbf{x}_R = (x_R, y_R)$ in the AT-INSAR image plane. In the particular case of range traveling waves, system operating in mode 1, it holds that $x = x_R$ and $y_R = y - B/2$.

2.2. The AT-INSAR Velocity Bunching Model

Instead of $I(\mathbf{x}_R)$, we consider $I_{vb}(\mathbf{x}_R)$ from the AT-INSAR Velocity Bunching Model. The derivation is presented in Bao et al. (1997). The basic facts as follow.

In this model, the AT-INSAR (single-look) integration time T_0 is at least one order of magnitude smaller than the period of the dominant ocean wave. So, both the normalized radar cross section $\sigma(\mathbf{x}, t)$ and the radial velocity $u_r(\mathbf{x}, t)$ show a small variation with respect to time. This allows an approximation of these values by the respective quantities $\sigma_0(\mathbf{x})$ and $u_r(\mathbf{x})$, which are independent of time. In the particular case of the radial velocity, a first order approximation in time around $t_0 = \mathbf{x}/V$ is used:

$$u_r(\mathbf{x}, t) \approx u_r(\mathbf{x}) + a_r(\mathbf{x})(t - t_0)$$

here, $a_r(\mathbf{x})$ denotes the radial acceleration (at $\mathbf{x}$) that is associated with the ocean surface. In our modeling, both $u_r(\mathbf{x})$ and $a_r(\mathbf{x})$ are in the same order of magnitude (Holthuijsen, 2007).

With these considerations, the expression for $I_{vb}(\mathbf{x}_R)$ is:

$$\begin{aligned} I_{vb}(\mathbf{x}_R) = {} & \frac{\pi T_0^2 \rho_a}{2} \exp\left[-\frac{4B^2}{V^2 T_0^2}\right] \int_{-\infty}^{+\infty} \frac{\sigma_0(\mathbf{x})}{\rho'_a(\mathbf{x})} \\ & \times \exp\left[-2jk_r \frac{B}{V} u_r(\mathbf{x})\right] \exp\left[\frac{4B^2\rho_a^2}{V^2 T_0^2 \rho'^2_a(\mathbf{x})}\right] \\ & \times \exp\left[\frac{2jBk_r}{R}\left(\frac{2\rho_a^2}{\rho'^2_a(\mathbf{x})} - 1\right)\left(y_R - y - \frac{R}{V}u_r(\mathbf{x})\right)\right] \\ & \times \exp\left[-\frac{\pi^2}{\rho'^2_a(\mathbf{x})}\left(y_R - y - \frac{R}{V}u_r(\mathbf{x})\right)^2\right] dy \end{aligned} \tag{1}$$

$$\rho'_a(\mathbf{x}) = \left\{\rho_a^2 + \left[\frac{\pi}{2}\frac{T_0 R}{V} a_r(\mathbf{x})\right]^2 + \frac{\rho_a^2 T_0^2}{\tau_s^2}\right\}^{1/2}$$

where,

- k_r denotes the wavenumber of the incoming electromagnetic wave,
- λ_r denotes the radar wavelength, that is, $\lambda_r = (2\pi)/k_r$,
- $\rho_a = \lambda_r R/(2VT_0)$ is the single-look azimuthal resolution for stationary targets,
- $\rho'_a(\mathbf{x})$ is the degraded single-look azimuthal resolution, due to moving targets,
- τ_s denotes the scene coherence time.

Referring to the integral Equation 1, let A_0 denote its constant factor:

$$A_0 = \frac{\pi T_0^2 \rho_a}{2} \exp\left[-\frac{4B^2}{V^2 T_0^2}\right] \tag{2}$$

and let A_1 denote the azimuthal shift that contributes to the azimuthal smearing:

$$A_1 = y_R - y - \frac{R}{V} u_r(\mathbf{x}) \tag{3}$$

Using Equations 2 and 3, the integral Equation 1 can be written in this form:

$$\begin{aligned} I_{vb}(\mathbf{x}_R) = A_0 \int_{-\infty}^{+\infty} \frac{\sigma_0(\mathbf{x})}{\rho_a'(\mathbf{x})} \exp\left[-2jk_r \frac{B}{V} u_r(\mathbf{x})\right] \exp\left[\frac{4B^2\rho_a^2}{V^2 T_0^2 \rho_a'^2(\mathbf{x})}\right] \\ \times \exp\left[\frac{2jBk_r}{R}\left(\frac{2\rho_a^2}{\rho_a'^2(\mathbf{x})} - 1\right) A_1\right] \exp\left[-\frac{\pi^2}{\rho_a'^2(\mathbf{x})} {A_1}^2\right] dy \end{aligned} \tag{4}$$

Let f_{vb} denote the integrand in Equation 4. In the context of this integral equation, observe that the cross-track coordinate $x_R = x$ is constant in the domain of u_r, a_r, σ_0, f_{vb} and I_{vb}. Hence, the nonlinear oscillatory integral equation I_{vb} is one-dimensional, for each fixed x_R. Using the equivalences $u_r(y) \equiv u_r(\mathbf{x})$, $a_r(y) \equiv a_r(\mathbf{x})$, $\sigma_0(y) \equiv \sigma_0(\mathbf{x})$ and $I_{vb}(y_R) \equiv I_{vb}(\mathbf{x}_R)$, this integral Equation 4 can be written as follows:

$$I_{vb}(y_R) \;=\; A_0 \int_{-\infty}^{+\infty} f_{\mathrm{vb}}(u_r(y), a_r(y), \sigma_0(y), y, y_R)\, dy, \qquad \text{for each} \quad x_R = x. \tag{5}$$

2.3. Problem Statement

In practice, one has the $I_{vb}(\mathbf{x}_R)$ image corrupted by noise, say $D(\mathbf{x}_R)$. We are interested in the following inverse (imaging) problem:

> Given a noisy AT-INSAR image D of an unknown sea surface z, compute an approximation u_r^* of the corresponding scalar field of radial velocities u_r that is associated with z.

Figure 2 illustrates our general goal, which starts with $D \in \mathbb{C}^{N_y \times N_x}$ (left side), and ends with an approximation $u_r^* \in \mathbb{R}^{N_y \times N_x}$ (right-down).

For both D and u_r^*, every cross-track coordinate $x_R = x$ determines an azimuthal line (vertical line) that passes through all the azimuthal coordinates. The radial velocity u_r^* is constructed on each vertical line by solving the noisy version of the integral Equation 5. Hereafter, this is referred as an *(inversion) problem*.

Because there are N_x azimuthal lines, there are N_x inversion problems to be solved separately. Each x-coordinate inversion problem takes as input the x-coordinate azimuthal line of D, and its output is the solution that appears in the x-coordinate azimuthal line of u_r^*.

2.3.1. Newton's Method for the Nonlinear Integral Equation (NL)

Consider the function spaces $\mathcal{V}, \mathcal{W} \subset L^2((-\infty, \infty))$. The nonlinear integral equation that is given in Equation 5 implicitly defines a map $\mathcal{I}$ between $\mathcal{V}$ and $\mathcal{W}$, namely,

$$\mathcal{I} : \mathcal{V} \to \mathcal{W}, \quad u_r \mapsto \mathcal{I}(u_r) = I_{vb}.$$

In order to formulate the inversion problem as the solution to a nonlinear integral equation, we consider the residual map

$$\mathcal{F} : \mathcal{V} \to \mathcal{W}, \qquad \mathcal{F}(u_r) \;=\; D - \mathcal{I}(u_r),$$

The problem is to find the function $u_r^* \in \mathcal{V}$ such that

$$\mathcal{F}(u_r) \;=\; 0.$$

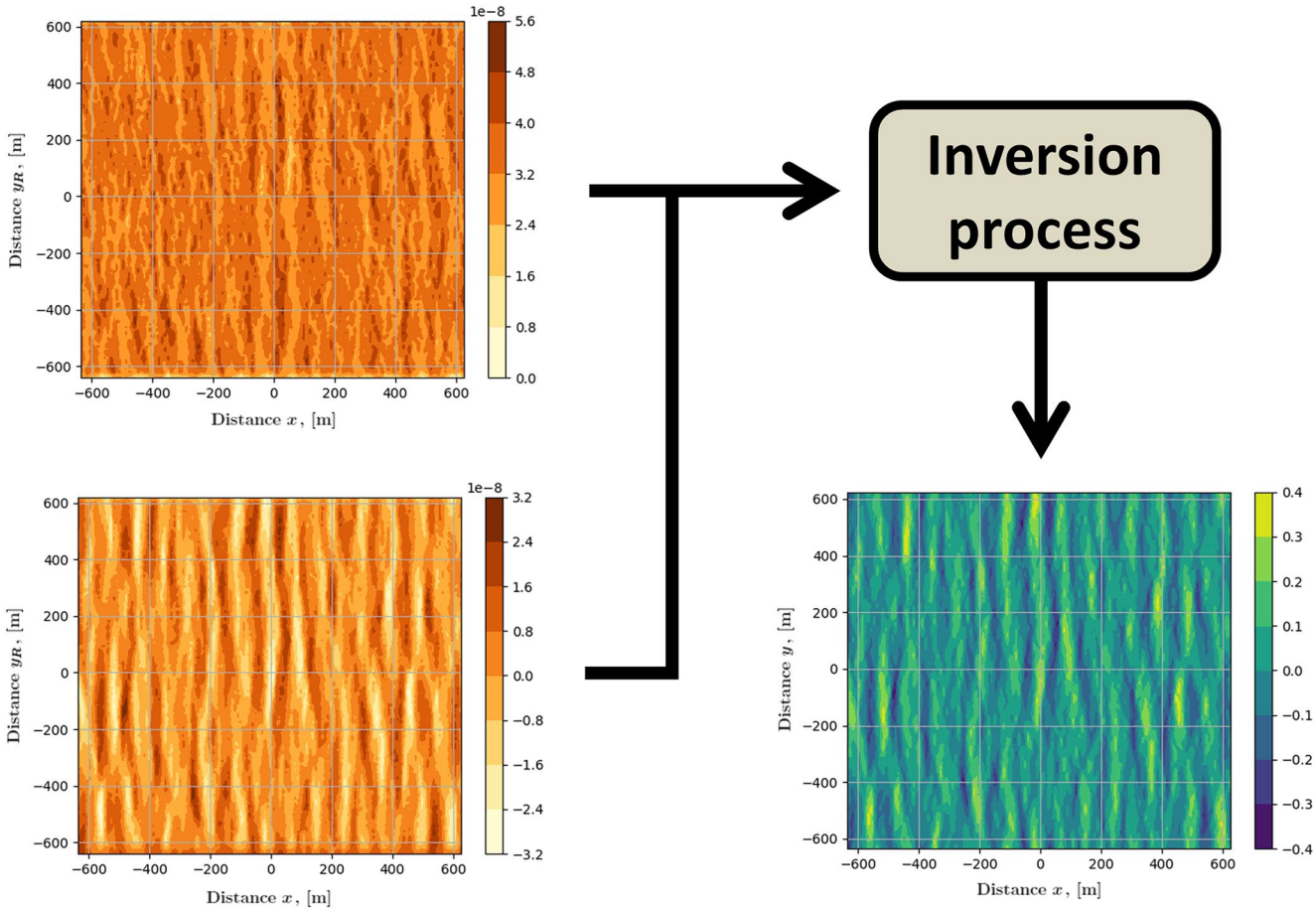

Figure 2. The inverse (imaging) problem. Left-top: Re$\{D\}$, left-down: Im$\{D\}$, right-down: u_r^*.

Assuming Fréchet differentiability, we apply the Newton's method.

Given the initial guess $u_r^0 \in \mathcal{V}$, we solve at each iteration k for $h^k \in \mathcal{V}$, and update:

$$\mathcal{F}'(u_r^k)\, h^k = -\mathcal{F}(u_r^k) \tag{6}$$

$$u_r^{k+1} \leftarrow u_r^k + h^k. \tag{7}$$

here, $\mathcal{F}'$ is the Fréchet derivative of $\mathcal{F}$. The mapping $\mathcal{F}'(u_r) : \mathcal{V} \to \mathcal{W}$ is defined as

$$\mathcal{F}'(u_r) = -\mathcal{I}'(u_r), \qquad \text{and}$$

$$\mathcal{I}'(u_r)h = I'_{vb}(h) = A_0 \int_{-\infty}^{\infty} \left[\frac{\partial f_{vb}}{\partial u_r}\right] h(y)\, dy$$

where $(\partial f_{vb}/\partial u_r)$ is the vector calculus derivative of f_{vb} with respect to u_r:

$$\frac{\partial f_{vb}}{\partial u_r} = \left[\frac{2\,\pi^2 R\, A_1 - j\,4\,B\,k_r\,\rho_a^2}{V\,\rho_a'^2}\right] f_{vb}$$

We remark that the scheme (6), (7) is the continuous (infinite dimensional) version of the Newton's method.

Subsequently, we discretize with an appropriate quadrature to obtain a finite dimensional residual $F : \mathbb{R}^{N_y} \to \mathbb{R}^{2N_y}$.

Given an initial guess $\vec{u}_r{}^0 \in \mathbb{R}^{N_y}$, we solve at each iteration k for $\vec{h}^k \in \mathbb{R}^{N_y}$, and update:

$$F'(\vec{u}_r{}^k)\,\vec{h}^k = -F(\vec{u}_r{}^k)$$
$$\vec{u}_r{}^{k+1} \leftarrow \vec{u}_r{}^k + \vec{h}^k \tag{8}$$

The linear system (Equation 8), to be solved in each iteration, is overdetermined and ill conditioned. Thus, its numerical solution is somewhat challenging.

We apply Tikhonov regularization using the SVD of $F'(\vec{u}_r{}^k)$, namely,

$$\vec{h}^k \approx \vec{h}^k_{\alpha_T} = -\sum_{i=1}^{N_y} \frac{\sigma_i}{\sigma_i^2 + \alpha_T} \left[\vec{u}_i \cdot F(\vec{u}_r{}^k)\right] \vec{v}_i$$

where $\sigma_i \in \mathbb{R}_{\geq 0}$ is the i-th largest singular value of $F'(\vec{u}_r{}^k)$, $\vec{u}_i \in \mathbb{R}^{2N_y}$ is the corresponding i-th left singular vector, and $\vec{v}_i \in \mathbb{R}^{N_y}$ is the corresponding i-th right singular vector.

This regularization technique is classical, see Vogel (2002). The problem strives on the choice of the regularization parameter for a successful application. Here, the parameter is set to the square of the first (and largest) singular value of $F'(\vec{u}_r{}^k)$:

$$\alpha_T \leftarrow \sigma_1^2$$

Remark The Newton's method is initially applied to both u_r and a_r for the corresponding residual map $\mathcal{F}(u_r, a_r)$. In our case study, it is found a fortiori, that the derivative of $\mathcal{F}$ with respect to the radial acceleration is negligible. Consequently, the terms involving the latter in the Newton's methods are discarded. It is possible to show this mathematically, but in this work we will only focus on the numerical results.

2.4. A Functional Minimization Approach (FM)

For comparison, we develop a descent method for the corresponding nonlinear squares problem. The underlying functional,

$$\mathcal{G} : \mathcal{V} \to [0, \infty),$$

is given by

$$\mathcal{G}(u_r) = \frac{1}{2}\|\mathcal{F}(u_r)\|^2 = \frac{1}{2}\langle \mathcal{F}(u_r), \mathcal{F}(u_r)\rangle$$

Here, we formulate the inversion problem as the minimization of $\mathcal{G}$:

$$\min_{u_r \in \mathcal{V}} \; \mathcal{G} : \mathcal{V} \to [0, \infty)$$

It is readily seen that the Fréchet derivative of $\mathcal{G}$ at u_r applied to h is:

$$\mathcal{G}'(u_r)h \;=\; \frac{1}{2}\left[\langle h, (\mathcal{F}'(u_r))^*\mathcal{F}(u_r)\rangle + \overline{\langle h, (\mathcal{F}'(u_r))^*\mathcal{F}(u_r)\rangle}\right]$$

where $(\mathcal{F}'(u_r))^*$ is the adjoint operator of $\mathcal{F}'(u_r)$. Hence,

$$\mathcal{G}'(u_r)h = \left\langle h,\ \mathrm{Re}\left\{(\mathcal{F}'(u_r))^*\mathcal{F}(u_r)\right\}\right\rangle$$

Substituting $\mathcal{F}'(u_r)$, it follows that

$$\mathcal{G}'(u_r)h \;=\; \left\langle h, \mathrm{Re}\left\{-A_0 \int_{-\infty}^{\infty} \left[\frac{\partial f_{vb}}{\partial u_r}\right] \overline{\left[\mathcal{F}(u_r)\right](y_R)}\, dy_R \right\}\right\rangle$$

Table 1
Ocean Surface Parameters

Description	Name	Value	Units	Parameter
Wind speed	U_{10}	5	[m s^{-1}]	Input
Peak wavelength	λ_S	100	[m]	Input
Peak wave period	T_S	8.004415	[s]	Derived

By the Riesz representation theorem, the second argument of the inner product is the continuous gradient of $\mathcal{G}$ at u_r. That is, the function $\nabla\mathcal{G}(u_r)$ is defined as:

$$\nabla\mathcal{G}(u_r) = \mathrm{Re}\left\{-A_0\int_{-\infty}^{\infty}\left[\frac{\partial f_{vb}}{\partial u_r}\right]\overline{\left[\mathcal{F}(u_r)](y_R)\right]}\,dy_R\right\} \tag{9}$$

The minimization problem is solved by the BFGS method with known gradient. In our case, a discrete version of Equation 9.

3. Synthetic Data

In this section, we specify the parameters and functions that we have employed to simulate the ocean surface and its associated AT-INSAR data. The area under study is a square Q with 1,280 meters of side length, centered at the origin. We consider a 128×128 uniform square mesh, whose computation points lie at their vertices. Using this area with its mesh, the simulated ocean surface is $z : Q \to \mathbb{R}$, and its associated AT-INSAR data is $D : Q \to \mathbb{C}$.

3.1. Sea Surface

We have developed our own software for ocean surface simulation. We follow the classical variance spectra to surface approach, to generate a random 2-D realization of a sea surface, see Mobley (2016). We adopt the configuration given in Bao et al. (1997). Table 1 shows ocean surface parameters.

Since our basis for comparison is Brüning et al. (1990), we consider a swell sea described by the highly peaked JONSWAP omnidirectional spectrum introduced therein. Namely,

$$\mathcal{S}_S(k) = \frac{\alpha_S}{2\,k^3}\exp\left[-\frac{5}{4}\left(\frac{k}{k_S}\right)^{-2}\right]\gamma_S{}^{G_S}$$

where

$$G_S = \exp\left[-\frac{1}{2}\,\frac{(k^{1/2} - k_S^{1/2})^2}{\sigma_S^2\,k_S}\right]$$

here,

- $\alpha_S = 0.212 \times 10^{-3}$ is the energy scale of $\mathcal{S}_S$.
- $k_S = (2\pi)/\lambda_S$ is the spatial peak frequency of $\mathcal{S}_S$.
- $\gamma_S = 10$ is the peak enhancement factor of $\mathcal{S}_S$.
- σ_S is the spectral width centered at k_S,

$$\sigma_S = \begin{cases} 0.07 & \text{for} \quad k \le k_S \\ 0.09 & \text{for} \quad k > k_S \end{cases}$$

In the frequency domain, Figure 3 depicts the omnidirectional spectrum $\mathcal{S}_S$, whose narrow shape—centered at low frequencies—constitutes the underlying model that generates a swell sea state in the space-time domain. This spectrum $\mathcal{S}_S$ corresponds to one of the sea state configurations that are proposed in Brüning et al. (1990), which in turn is adopted by Bao et al. (1997) in its AT-INSAR imaging problem of ocean waves.

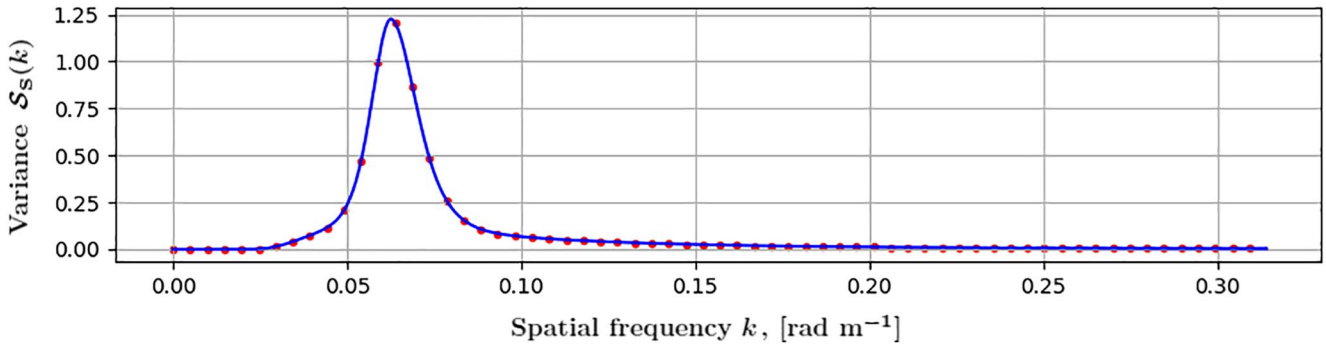

Figure 3. Omnidirectional spectrum $\mathcal{S}_S$: continuous (line) and sampled (dots).

Next, a spreading function is used. In this case, the two-sided cosine-power model,

$$\Phi_{\text{cp2}}(k,\phi) \;=\; \frac{1}{2}\,N_p\,|\cos(\phi-\phi_w)|^{2p}, \qquad |\phi-\phi_w| \;\le\; \pi,$$

Leading to the two-sided directional swell spectrum,

$$\mathcal{S}_{2C}(k_x,k_y) \;=\; \frac{1}{k}\,\mathcal{S}_S(k)\,\Phi_{\text{cp2}}(k,\phi),$$

where (k, ϕ) and (k_x, k_y) are the equivalent polar and cartesian coordinates, respectively.

We obtain a particular instance of the ocean variance spectrum $\hat{z}$. The ocean surface z is obtained by computing the discrete inverse Fourier transform of $\hat{z}$.

3.2. The AT-INSAR Data

Table 2 shows the values that are given to the input parameters for the configuration of the AT-INSAR system. This selection is based on part III-B of Bao et al. (1997).

Based on Table 2 and the ocean variance spectrum $\hat{z}$, we show a relevant set of derived parameters and functions in Table 3. This configuration allows the construction of the discrete scalar fields of ocean-radar interaction: the radial velocities u_r, the radial accelerations a_r, and the time-averaged radar reflectivities σ_0.

From the information of Table 3, the intensity $I_{vb}(\mathbf{x}_R)$ is approximated by quadrature.

Our modeling study is within the scope of inverse problems theory. As customary, see Estatico et al. (2015), we consider additive noise at each $\mathbf{x}_R$.

More precisely, to generate synthetic data, we add to $I_{vb}(\mathbf{x}_R)$ noise $\eta(\mathbf{x}_R)$ given by

$$\eta(\mathbf{x}_R) = \frac{1}{\sqrt{2}}\left[a_\eta(\mathbf{x}_R) \;+\; j\,b_\eta(\mathbf{x}_R)\right],$$

where the elements $a_\eta(\mathbf{x}_R)$ and $b_\eta(\mathbf{x}_R)$ are independent, identically distributed, real Gaussian random variables, with mean 0 and variance $\sigma_\eta^2(\mathbf{x}_R)$.

The location-dependent standard deviation $\sigma_\eta(\mathbf{x}_R)$ is given by

$$\sigma_\eta(\mathbf{x}_R) = \varepsilon \;\; \max\{|I_{\text{vb}}(\mathbf{x}_R)|, \;\; \text{LB}\}$$

We set $\varepsilon = 0.05$, allowing a 5% Gaussian error. LB $= 1 \times 10^{-10}$ is about the same order of magnitude of $I_{vb}(\mathbf{x})$. This latter is introduced to avoid point supported densities.

Table 2
Input Parameters to Configure the AT-INSAR System

Description	Name	Value	Units
Angle of incidence	θ_r	$\pi/4$	[rad]
Platform speed	V	200	[m s^{-1}]
Carrier frequency	f_0	1.25×10^9	[s^{-1}]
Target exposure time	T_0	0.751	[s]
Half the distance between antennas	B	9.8	[m]
Scene coherence time	τ_s	0.12	[s]
Radar polarization (like-polarized)	VV	–	–

Table 3
Derived Parameters and Functions of the AT-INSAR System

Description	Name	Value	Units
Radar wavelength	λ_r	0.239834	[m]
Radar wavenumber	k_r	26.19806	[rad m^{-1}]
Antenna length (in azimuth)	L_a	21.22099	[m]
Time separation between antennas	Δt	0.049	[s]
Field of radial velocities	u_r	$u_r[\mathbf{x}_R]$	[m s^{-1}]
Field of radial accelerations	a_r	$a_r[\mathbf{x}_R]$	[m s^{-2}]
Field of radar reflectivities	σ_0	$\sigma_0[\mathbf{x}_R]$	[1]

Consequently, the noisy AT-INSAR data D is given by

$$D(\mathbf{x}_R) = I_{vb}(\mathbf{x}_R) + \eta(\mathbf{x}_R)$$

3.3. Interferometric Velocities

Given the noisy AT-INSAR image D, the interferometric phase Φ_{ATI} is $\Phi_{ATI} = \angle D$, the latter is proportional to the interferometric velocity u_{ATI} (Bamler & Hartl, 1998; Goldstein & Zebker, 1987):

$$u_{ATI}(\mathbf{x}) = -\frac{\lambda_r}{4\pi}\frac{V}{B}\Phi_{ATI}(\mathbf{x}_R).$$

In applications, u_{ATI} is used as an approximation of the radial velocity u_r. We gauge this approximation in the results that follow.

4. Numerical Results

For radial velocity imaging, we consider two main configurations: RTW and ATW. In the former, both tilt and hydrodynamic modulations of the ocean surface are specially stronger, whereas azimuthal smearing and velocity bunching of the ocean surface are particularly stronger in the latter.

In Appendix A we shall present results for variations of both RTW and ATW, which consists of a different wind direction ϕ_w and two additional R/V ratios. Here we fully report the *RTW scenario*, which is based on section III-B of Bao et al. (1997).

Table 4 shows the particular values that characterize this scenario. Figure 4 depicts its most relevant fields and spectra. Note that the angle ϕ_0 [rad] given here corresponds to the angle $\phi_p = \phi_w - \phi_0 + \pi/2$ [rad] given in Bao et al. (1997).

As we show in Figure 4b, some properties of the ocean surface z are evident: there is a regular pattern of waves whose directions are very close to the wind direction $\phi_w = 0$ [rad], the majority of wavelengths are around $\lambda_S = 100$ [m], and a big amount of measured wave heights is well characterized by $\hat{H}_{m_0} = 0.586215$ [m].

4.1. Radial Velocity Imaging

Given $D(\mathbf{x}_R)$ for each x_R (cross-track coordinate) we employ, to solve for $u_r(\mathbf{x})$, both the Nonlinear System (NL) and the Functional Minimization (FM), which are associated with the nonlinear integral equation. In total there are $N_x = 128$ problems ordered from left to right, from 0 to 127. We stress that we follow the optimize then discretize approach. For comparison, we use the discretize then optimize in the minimization problem. Results with the latter shall be referred as DFM.

Table 4
The RTW Scenario: Input and Derived Parameters

Description	Name	Value	Units	Parameter
Wind direction	ϕ_w	0	[rad]	Input
Azimuthal look direction	ϕ_0	0	[rad]	Input
Slant range	R	15×10^3	[m]	Input
Range-to-velocity ratio	R/V	75	[s]	Derived
Variance of surface elevation	$\mathrm{Var}\{z(\mathbf{x}_R, t)\}$	0.020575	[m^2]	Derived
Sample variance of z	s_z^2	0.021478	[m^2]	Derived
Sample significant wave height	$\hat{H}_{m_0}$	0.586215	[m]	Derived
Azimuth SAR resolution	ρ_a	11.97573	[m]	Derived
Vector of radar LOS	v_{LOS}	$\left[\frac{\sqrt{2}}{2}, 0, -\frac{\sqrt{2}}{2}\right]^T$	unitary	Derived

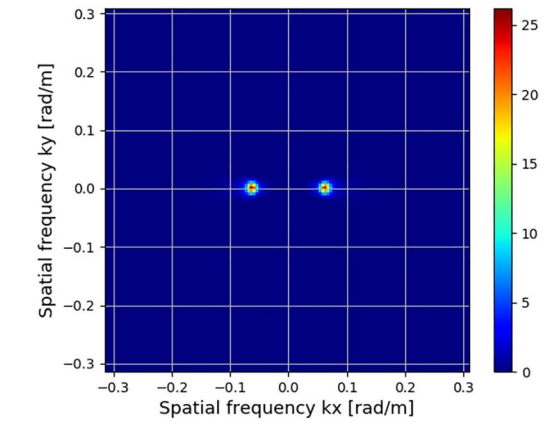

(a) Sampled directional spectrum $\hat{\mathscr{S}}_{2C}$.

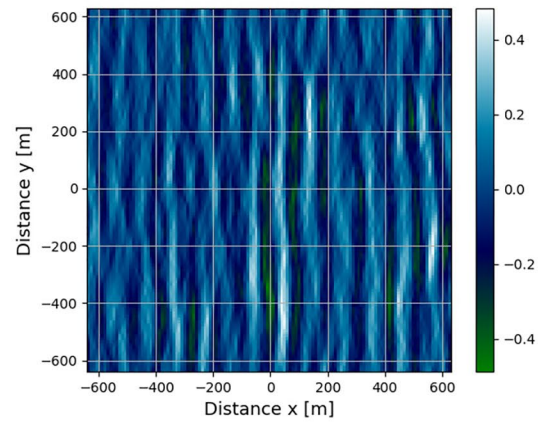

(b) The simulated ocean surface z.

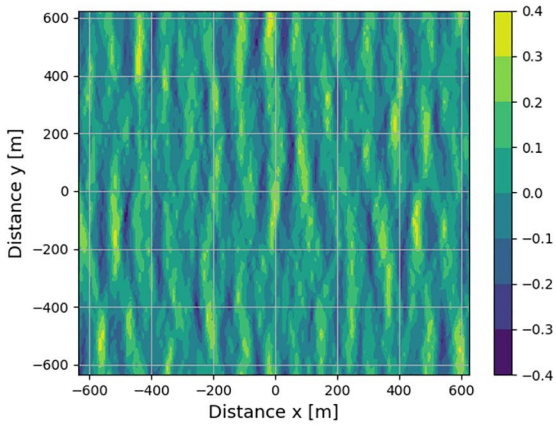

(c) Field of radial velocities u_r.

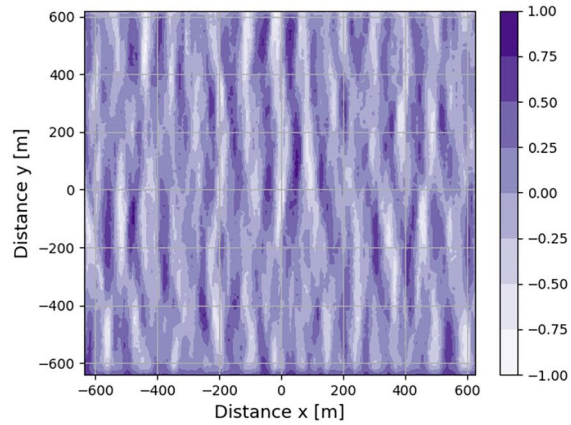

(d) The phase $\Phi_{ATI} = \angle D$.

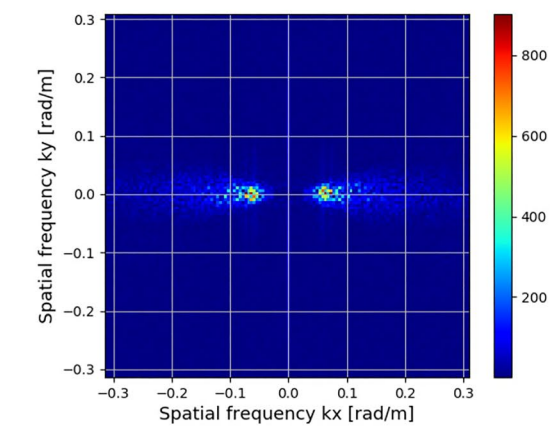

(e) The spectrum $\mathfrak{F}_D\{\Phi_{ATI}\}$.

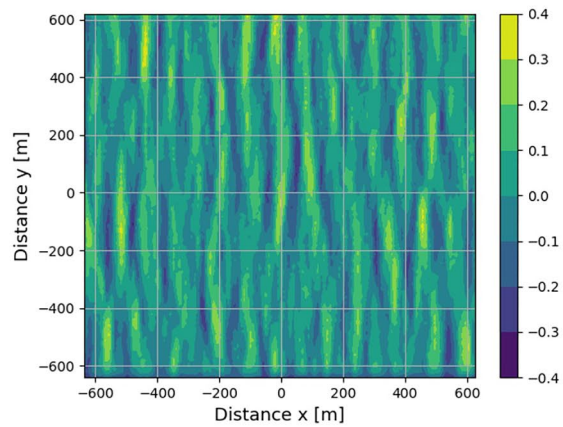

(f) The field u_{ATI}.

Figure 4. The RTW scenario: (a) is the spectrum $\mathscr{S}_{2C}$, (b) is the ocean surface z, (c) is the field u_r, (d) is the phase Φ_{ATI}, (e) is the spectrum $\mathfrak{F}_D\{\Phi_{ATI}\}$, (f) is the field u_{ATI}.

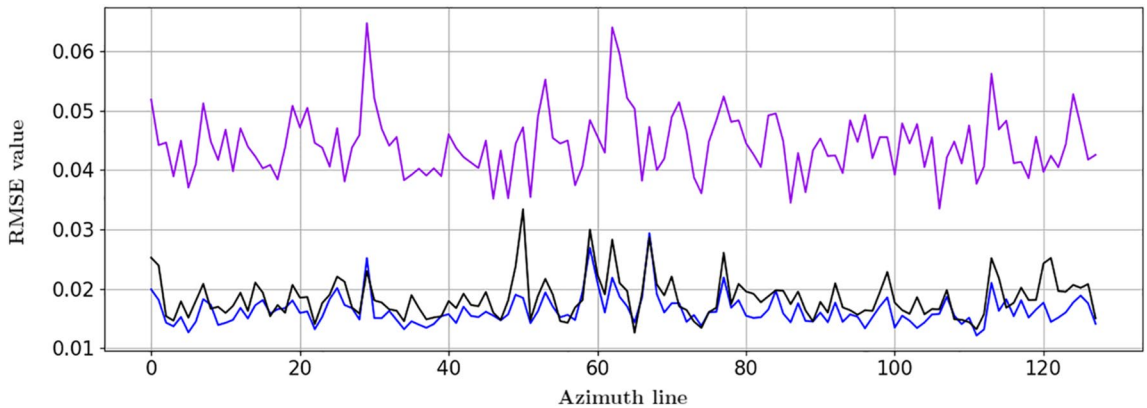

Figure 5. Root Mean Square Error values. Blue: u_r^*–NL, Black: u_r^*–DFM, Violet: u_{ATI}. Each abscissa is a problem.

In the minimization problems, the main difference is the computation of the gradient. In the infinite dimensional, optimize then discretize approach, the gradient is analytic and is given by the Equation 9. In the discretize then optimize formulation, the gradient is approximated with appropriate finite differences of the discretized (finite dimensional) functional.

To avoid bias, we start all iterative methods with $u_r^0 \equiv 0$ as initial guess.

Summarizing, for each optimization problem, we compute the following four solutions:

1. The Nonlinear System solution, denoted by u_r^*–NL.
2. The Continuous Functional Minimization solution, denoted by u_r^*–FM.
3. The Discrete Functional Minimization solution, denoted by u_r^*–DFM.
4. The interferometric velocity solution, denoted by u_{ATI}.

To show a global comparison, we compute the Root Mean Square Error (RMSE) of each solution with respect to the target u_r. In Figures 5 and 6, we exhibit such comparison for each optimization problem (each abscissa is an azimuth line that corresponds to a problem).

From Figure 5, it is apparent that NL performs better than DF. From Figure 6, we can see that both FM and FDM have a very similar performance, which means that their accuracies are quite comparable. Finally, both Figures 5 and 6 confirm an important result: for each optimization problem, every optimization strategy (NL, FM or FDM) outperforms the interferometric velocity of Goldstein and Zebker (1987).

In the following numerical results, we employ a specific figure to show the solution of a particular problem via a particular strategy. More specifically, the figure contains the fit for the radial velocity (using a particular strategy)

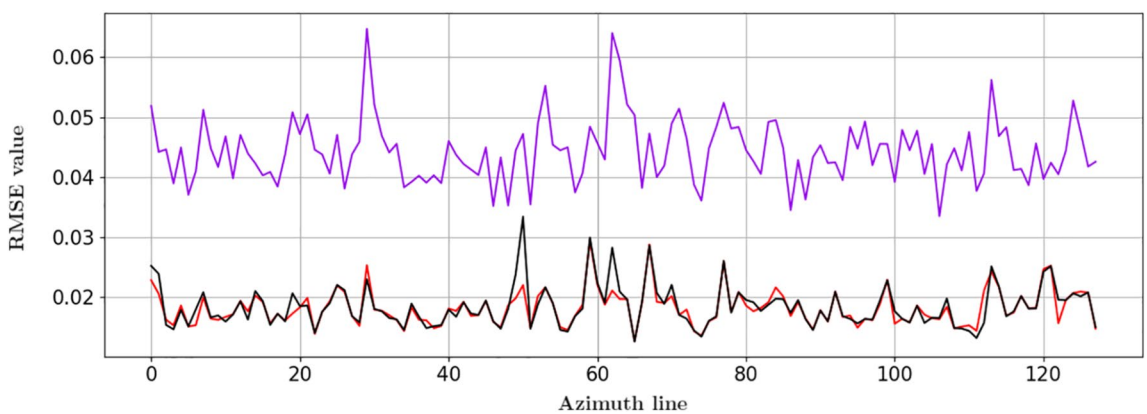

Figure 6. Root Mean Square Error values. Red: u_r^*–FM, Black: u_r^*–DFM, Violet: u_{ATI}. Each abscissa is a problem.

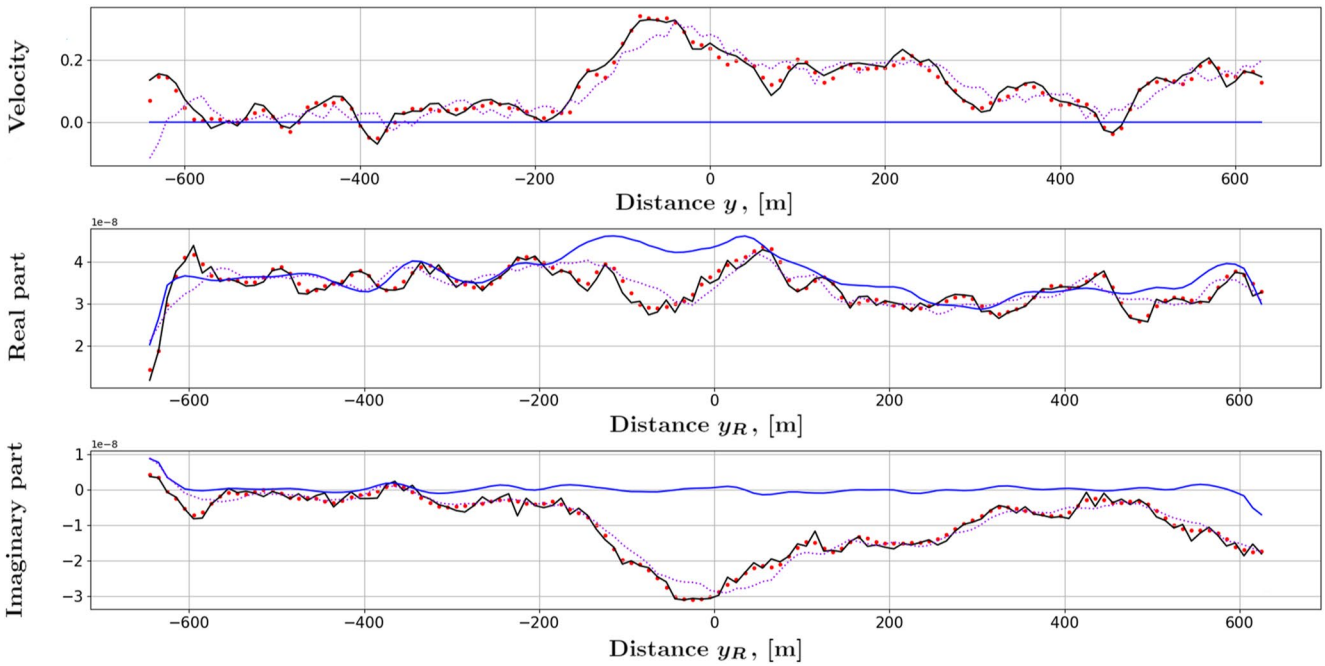

Figure 7. Problem 64 via NL. Top: radial velocity u_r (black), initial point u_r^0 (blue), interferometric velocity u_{ATI} (violet), estimated radial velocity u_r^* (red); Middle: Re $\{D\}$ (black), Re $\{I_0\}$ (blue), Re $\{I_{ATI}\}$ (violet), Re $\{I_*\}$ (red); Bottom: Im $\{D\}$ (black), Im $\{I_0\}$ (blue), Im $\{I_{ATI}\}$ (violet), Im $\{I_*\}$ (red).

and its associated AT-INSAR image I (the forward mapping). In each figure, and for comparison purposes, we have also included the interferometric velocity solution u_{ATI}. We show the fitting results for problem 64.

Figures 7 and 8 are related to the same problem 64: Figure 7 presents the result via the Nonlinear System solution u_r^*–NL, whereas Figure 8 presents the result via the Continuous Functional Minimization solution u_r^*–FM.

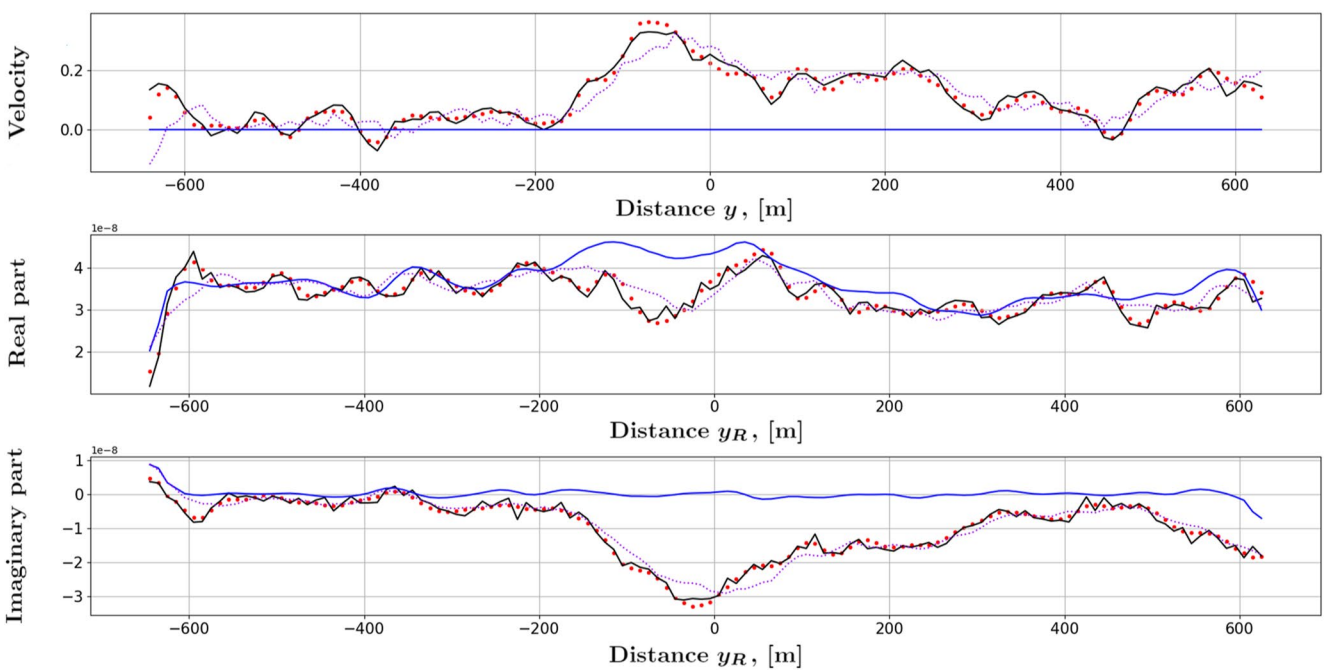

Figure 8. Problem 64 via FM. Top: radial velocity u_r (black), initial point u_r^0 (blue), interferometric velocity u_{ATI} (violet), estimated radial velocity u_r^* (red); Middle: Re $\{D\}$ (black), Re $\{I_0\}$ (blue), Re $\{I_{ATI}\}$ (violet), Re $\{I_*\}$ (red); Bottom: Im $\{D\}$ (black), Im $\{I_0\}$ (blue), Im $\{I_{ATI}\}$ (violet), Im $\{I_*\}$ (red).

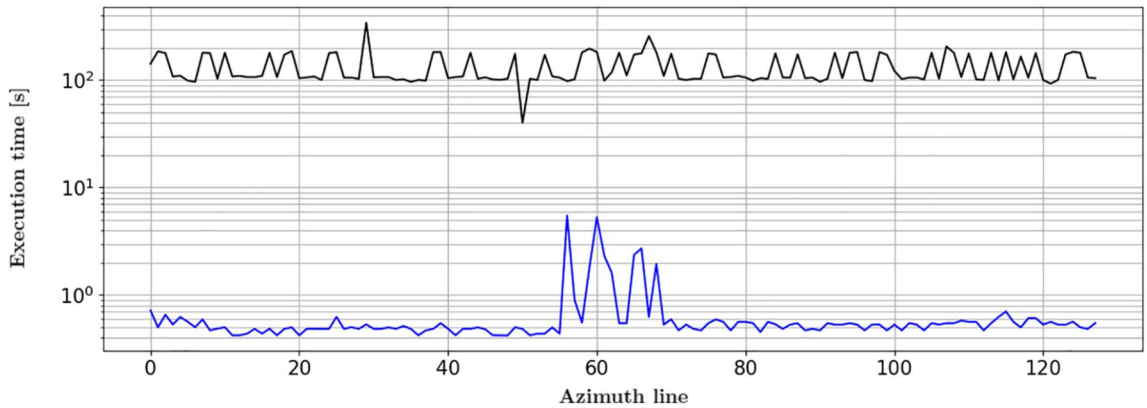

Figure 9. Execution times. Blue: u_r^*–NL, Black: u_r^*–DFM. Each abscissa is a problem.

For the interested reader, our exhaustive numerical experiments are available in the Marine Data Archive (MDA) repository, in accordance with the Data Availability Statement that we have provided below. It is apparent that results are remarkably consistent in all RTW and ATW configurations for the 128 problems.

4.2. Computational Efficiency

In practice, imaging problems are computationally expensive. In the discretize then optimize approach, the approximation of derivatives by finite differences is costly. Having the exact derivative, and postponing discretization *until the last moment*, the solution is in general more efficient.

Indeed, consider for instance the minimization problem. In the discretize then optimize approach, the function u_r is approximated by a vector $\vec{u}_r \in \mathbb{R}^{N_y}$. Let J denote the corresponding discrete minimization functional defined on $\mathbb{R}^{N_y}$, and $\vec{e}^j$ a standard basis vector. The simplest approximation of the partial derivative of J with respect to the j-th variable is the quotient

$$\frac{J(\vec{u}_r + h\vec{e}^j) - J(\vec{u}_r)}{h}.$$

Consequently, given $J(\vec{u}_r)$, to compute the gradient ∇J, N_y extra evaluations of J are necessary. Each evaluation amounts to the quadrature of an integral. In contrast, in the optimize then discretize approach, only one quadrature for Equation 9 is required.

We can see this advantage in Figures 9 and 10, where we report the values of execution time for the 128 inversion problems: in Figure 9, we show the comparison between the solutions u_r^*–NL and u_r^*–DFM; in Figure 10, we show

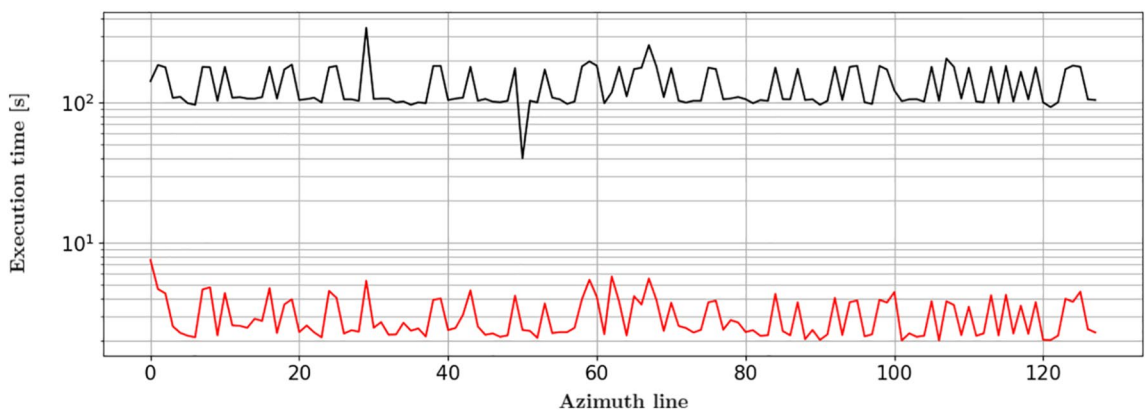

Figure 10. Execution times. Red: u_r^*–FM, Black: u_r^*–DFM. Each abscissa is a problem.

Table 5
Relative Errors of Kinetic Energies Associated With Three Estimated Solutions

Estimated solution	u_r^*–NL	u_r^*–FM	u_{ATI}
RE-KE of estimated solution	0.0630604	0.0130545	0.1240790

the comparison between the solutions u_r^*–FM and u_r^*–DFM. Note that both NL and FM are at least one order of magnitude faster than DFM.

4.3. A Physical Comparison

A first inspection of radial velocity fitting and AT-INSAR images (Figures 7 and 8), the gain with respect to the interferometric velocity u_{ATI} may seem marginal. To compare in terms of a physical quantity, we compute the relative error of kinetic energies (RE-KE) that are associated with the whole two-dimensional fields u_r^*–NL, u_r^*–FM and u_{ATI}. The results are shown in Table 5, where we see that the relative error of u_{ATI} is much greater than the relative errors of both u_r^*–NL and u_r^*–FM. The error of using u_{ATI} is about 12%, which might be critical in some applications.

5. Technical Information

For the simulation of the ocean surface realizations, the AT-INSAR images (forward mappings), and the functional versions of the Newton's methods (inverse mappings), we have developed our own software implementations from scratch. The comparative performance of the methods given above was carried out in a computer with the following specifications:

5.1. Hardware

- Processor: AMD © A10-5800B with Radeon(tm) HD Graphics, 3.80 GHz
- Physical memory: 8.00 Gb (7.20 Gb usable).
- Round-off unit (machine epsilon): $\varepsilon_M = 2.220446049250313 \times 10^{-16}$.

5.2. Software

- System type: 64-bit operating system.
- Operating system: Windows 7 Professional © 2009 – SP1, Microsoft Corporation.
- Programming language: Anaconda3 5.2.0 with Python 3.6.5 for 64 bits.
- Classical numerical methods (e.g., SVD and BFGS): NumPy and SciPy packages.
- IDE: The Scientific PYthon Development EnviRonment (Spyder) ©, version 3.2.8

6. Conclusions

Assuming the AT-INSAR-VB model, we have posed our problem—the estimation of radial velocities of a simulated ocean surface—as the solution to a nonlinear integral equation. To solve this equation, we have developed functional (infinite-dimensional) versions of two modified Newton's methods, namely, a nonlinear system method coupled with Tikhonov regularization, and the BFGS method with known gradient for functional minimization.

For each technique, we have formulated the solution on function spaces, where the application of the Newton's method requires the Fréchet derivative of the objective function.

We have implemented discrete models and numerical algorithms, which have led to numerical results that are satisfactory. The functional approach produces faster solutions when compared to the classical discretize then optimize strategy. Furthermore, the fitting of the estimated solutions of radial velocity improves upon the interferometric velocity u_{ATI} when the velocity bunching mechanism is a nonlinear process. Finally, the comparison of predicted kinetic energies shows that, for certain applications, a better fit other than interferometric velocities is required.

The proposed computational functional method has been tested successfully on six scenarios, three RTW and three ATW. We have used the resolution of Bao et al. (1997), a 128×128 grid. In terms of inversion problems (integral equation solutions), this amounts to 128 problems per surface. Consequently, reliability of the results is satisfactory. Of great interest is to continue in this line, carrying out a reliability study in the framework of

Statistical Signal Processing. Namely, generate statistical results from random tests, and to establish the Cramer-Rao lower bound (CRLB) for an alternative to evaluate accuracy performance of the proposed computational method. We aim to report on this elsewhere.

This research is manifold: ocean waves modeling, SAR imaging of sea surfaces, inverse problems, numerical optimization, computational methods, etcetera. Concerning the modeling of ocean waves, we have only considered a swell spectrum. But we know that JONSWAP and Pierson-Moskowitz spectra, for instance, are of interest as well. Also, the synthetic character of our input data may be regarded as a drawback. In fact, an imaging problem with actual data in a realistic test area is desired. However, a closer look to our methodology shows that the results mainly depend on the integral transform, and so the methods apply regardless of the test area. We would like to provide evidence of such numerical modeling in a later work.

Research on methods for sea surface imaging is ongoing. In a computational sense, the use of High Performance Computing is a straightforward continuation of this work. In our study, an integral equation is solved separately for each point in the cross track coordinate. This is because of the AT-INSAR-VB model, in which all the optimization problems are mutually independent. Consequently, a parallel implementation in a low-level computer language shall lead to even faster solutions.

Appendix A: Numerical Results for Different Directions and *R*/*V* Ratios

Now we show our results under five additional scenarios, whose common properties are given in Section 3.1 and Table 2. Each scenario is distinctive from the others because of three input parameters: the azimuthal look direction ϕ_0, the wind direction ϕ_w, and the slant range R. Their construction is based on sections III-B and III-E of Bao et al. (1997).

With ϕ_0, we can select different mechanisms of the ocean surface: in RTW, there is a stronger influence of tilt and hydrodynamic modulations; in ATW, there is a stronger influence of azimuthal smearing and velocity bunching. If ϕ_w is not parallel to neither range nor azimuth directions, the variations of RTW and ATW make each inversion problem more challenging, because the mechanisms of both directions get combined. If the ratio R/V increases, velocity bunching is stronger. See Alpers (1983), Bao et al. (1997), Brüning et al. (1990).

For each ATW-type scenario, every cross-track coordinate is $y_R = y$, which determines an *horizontal* azimuthal line, for both D and u_r^*. Thus, there are N_y inversion problems to be solved separately. This means that every y-coordinate inversion problem takes as input the y-coordinate azimuthal line (*horizontal line*) of D, and its output is the solution that appears in the y-coordinate azimuthal line (*horizonal line*) of u_r^*. Only for the single ATW scenario, we show the corresponding fitting results for its problem 64 (Figures A2 and A3). Results are similar for all other scenarios.

A1. The ATW Scenario

Table A1, Figure A1, Figure A2, Figure A3, Figure A4, Figure A5

Table A1
The ATW Senario: Input and Derived Parameters

Description	Name(s)	Value(s)	Units	Parameter
Wind direction	ϕ_w	0	[rad]	Input
Azimuthal look direction	ϕ_0	$\pi/2$	[rad]	Input
Slant range	R	15×10^3	[m]	Input
Range-to-velocity ratio	R/V	75	[s]	Derived
Variance of surface elevation	$\mathrm{Var}\{z(\mathbf{x}_R, t)\}$	0.020575	[m^2]	Derived
Sample variance of z	s_z^2	0.021478	[m^2]	Derived
Sample significant wave height	$\hat{H}_{m_0}$	0.586215	[m]	Derived
Azimuth SAR resolution	ρ_a	11.97573	[m]	Derived
Vector of radar LOS	v_{LOS}	$\left[0, \frac{\sqrt{2}}{2}, -\frac{\sqrt{2}}{2}\right]^T$	unitary	Derived

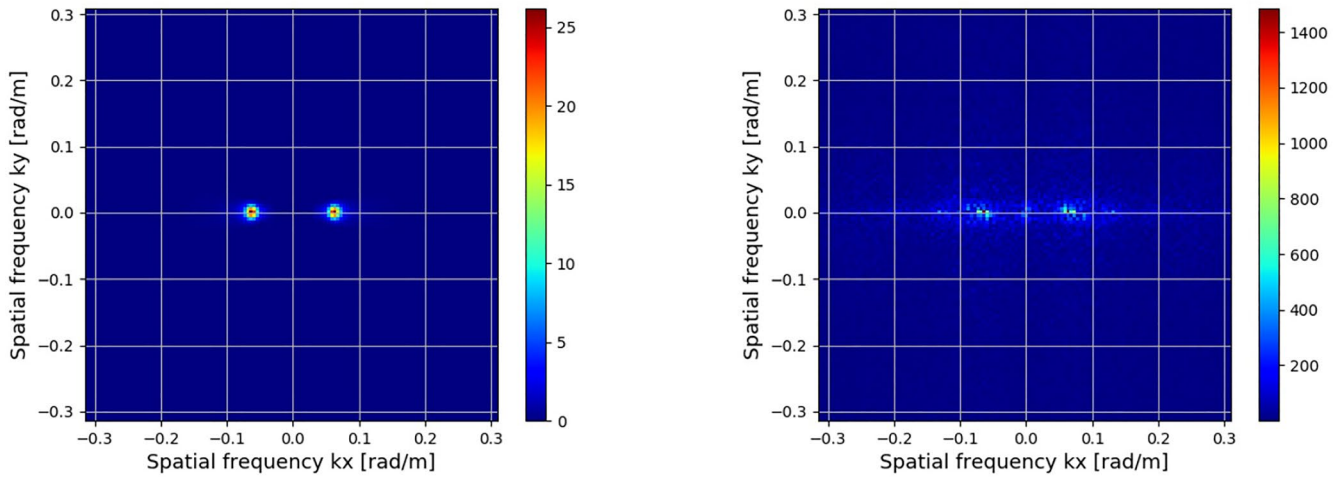

(a) Sampled directional spectrum $\hat{\mathscr{S}}_{2C}$. (b) The spectrum $\mathfrak{F}_D\{\Phi_{ATI}\}$.

Figure A1. The ATW scenario: the spectra $\hat{\mathscr{S}}_{2C}$ and $\mathfrak{F}_D\{\Phi_{ATI}.\}$.

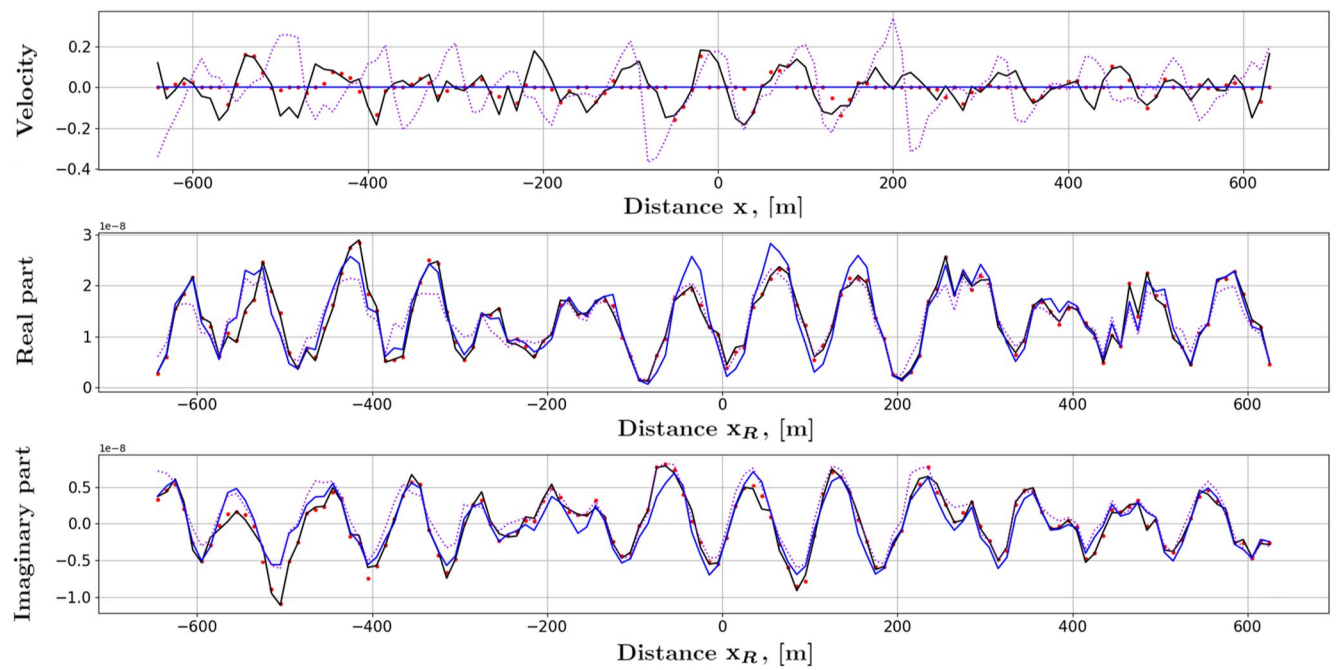

Figure A2. Problem 64 via NL. Top: radial velocity u_r (black), initial point u_r^0 (blue), interferometric velocity u_{ATI} (violet), estimated radial velocity u_r^* (red); Middle: Re $\{D\}$ (black), Re $\{I_0\}$ (blue), Re $\{I_{ATI}\}$ (violet), Re $\{I_*\}$ (red); Bottom: Im $\{D\}$ (black), Im $\{I_0\}$ (blue), Im $\{I_{ATI}\}$ (violet), Im $\{I_*\}$ (red).

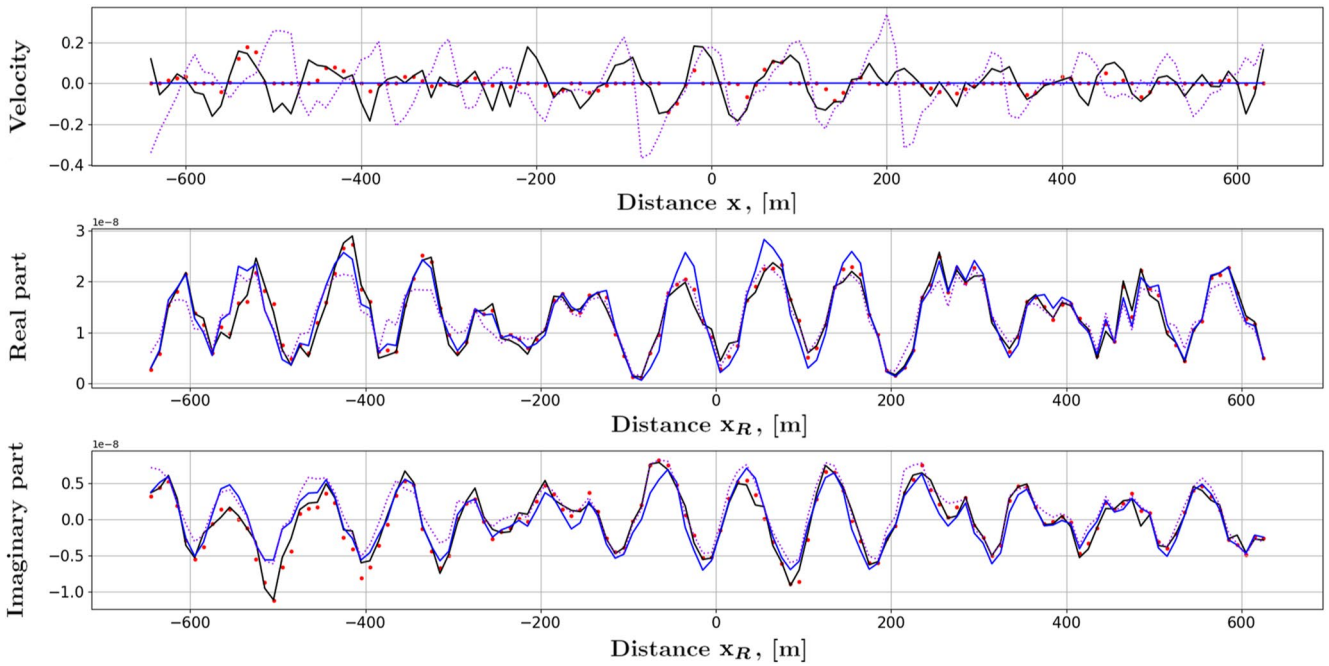

Figure A3. Problem 64 via FM. Top: radial velocity u_r (black), initial point u_r^0 (blue), interferometric velocity u_{ATI} (violet), estimated radial velocity u_r^* (red); Middle: Re $\{D\}$ (black), Re $\{I_0\}$ (blue), Re $\{I_{ATI}\}$ (violet), Re $\{I_*\}$ (red); Bottom: Im $\{D\}$ (black), Im $\{I_0\}$ (blue), Im $\{I_{ATI}\}$ (violet), Im $\{I_*\}$ (red).

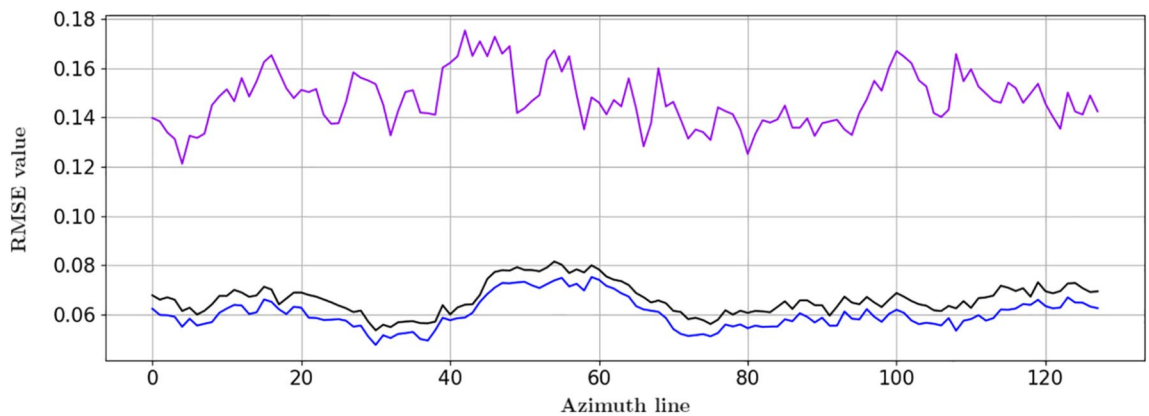

Figure A4. Root Mean Square Error values. Blue: u_r^*–NL, Black: u_r^*–DFM, Violet: u_{ATI}. Each abscissa is a problem.

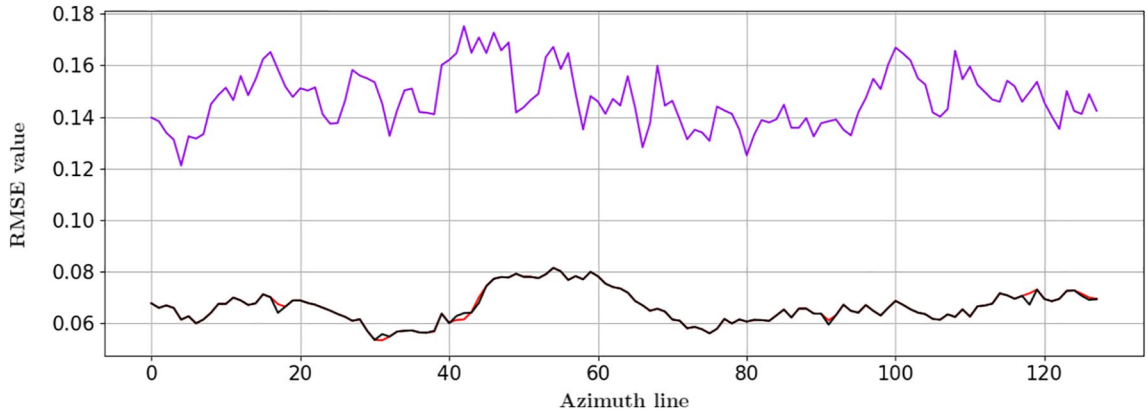

Figure A5. Root Mean Square Error values. Red: u_r^*–FM, Black: u_r^*–DFM, Violet: u_{ATI}. Each abscissa is a problem.

A2. The RTW-R16 Scenario

Table A2, Figure A6, Figure A7, Figure A8

Table A2
The RTW-R16 Scenario: Input and Derived Parameters

Description	Name(s)	Value(s)	Units	Parameter
Wind direction	ϕ_w	$\pi/9$	[rad]	Input
Azimuthal look direction	ϕ_0	0	[rad]	Input
Slant range	R	16×10^3	[m]	Input
Range-to-velocity ratio	R/V	80	[s]	Derived
Variance of surface elevation	$\mathrm{Var}\{z(\mathbf{x}_R, t)\}$	0.020620	[m^2]	Derived
Sample variance of z	s_z^2	0.016873	[m^2]	Derived
Sample significant wave height	$\hat{H}_{m_0}$	0.519591	[m]	Derived
Azimuth SAR resolution	ρ_a	12.77411	[m]	Derived
Vector of radar LOS	v_{LOS}	$\left[\frac{\sqrt{2}}{2}, 0, -\frac{\sqrt{2}}{2}\right]^T$	unitary	Derived

Note. First modification of R/V.

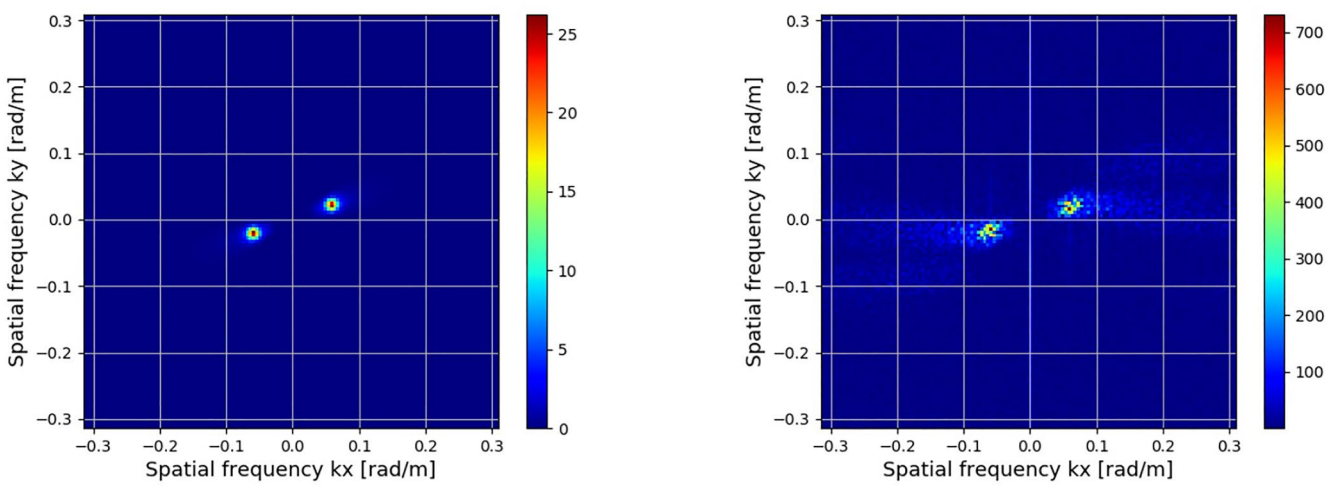

(a) Sampled directional spectrum $\hat{\mathscr{S}}_{2C}$. (b) The spectrum $\mathfrak{F}_D\{\Phi_{ATI}\}$.

Figure A6. The RTW-R16 scenario: the spectra $\hat{\mathscr{S}}_{2C}$ and $\mathfrak{F}_D\{\Phi_{ATI}.\}$.

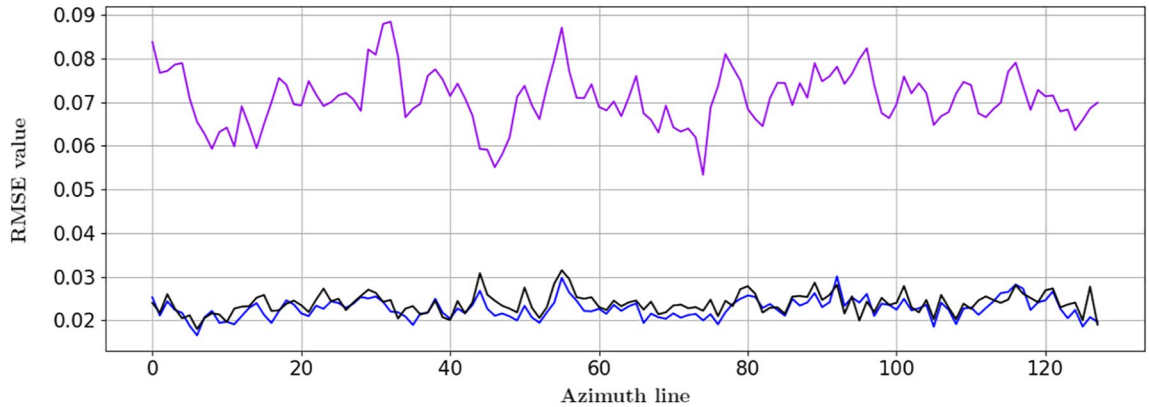

Figure A7. Root Mean Square Error values. Blue: u_r^*–NL, Black: u_r^*–DFM, Violet: u_{ATI}. Each abscissa is a problem.

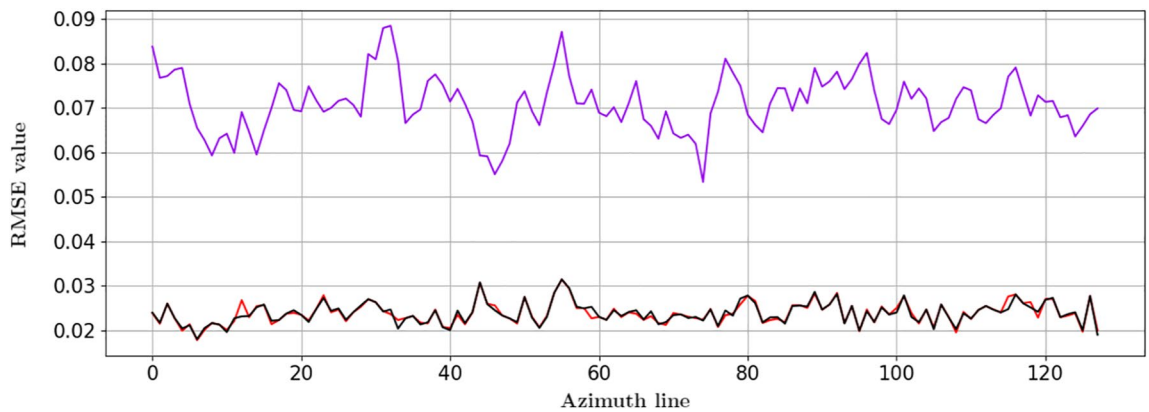

Figure A8. Root Mean Square Errorvalues. Red: u_r^*–FM, Black: u_r^*–DFM, Violet: u_{ATI}. Each abscissa is a problem.

A3. The RTW-R18 Scenario

Table A3, Figure A9, Figure A10, Figure A11

Table A3
The RTW-R18 Scenario: Input and Derived Parameters

Description	Name(s)	Value(s)	Units	Parameter
Wind direction	ϕ_w	$\pi/9$	[rad]	Input
Azimuthal look direction	ϕ_0	0	[rad]	Input
Slant range	R	18×10^3	[m]	Input
Range-to-velocity ratio	R/V	90	[s]	Derived
Variance of surface elevation	$\mathrm{Var}\{z(\mathbf{x}_R, t)\}$	0.020620	[m^2]	Derived
Sample variance of z	s_z^2	0.016873	[m^2]	Derived
Sample significant wave height	$\hat{H}_{m_0}$	0.519591	[m]	Derived
Azimuth SAR resolution	ρ_a	14.37087	[m]	Derived
Vector of radar LOS	v_{LOS}	$\left[\frac{\sqrt{2}}{2}, 0, -\frac{\sqrt{2}}{2}\right]^T$	unitary	Derived

Note. Second modification of R/V.

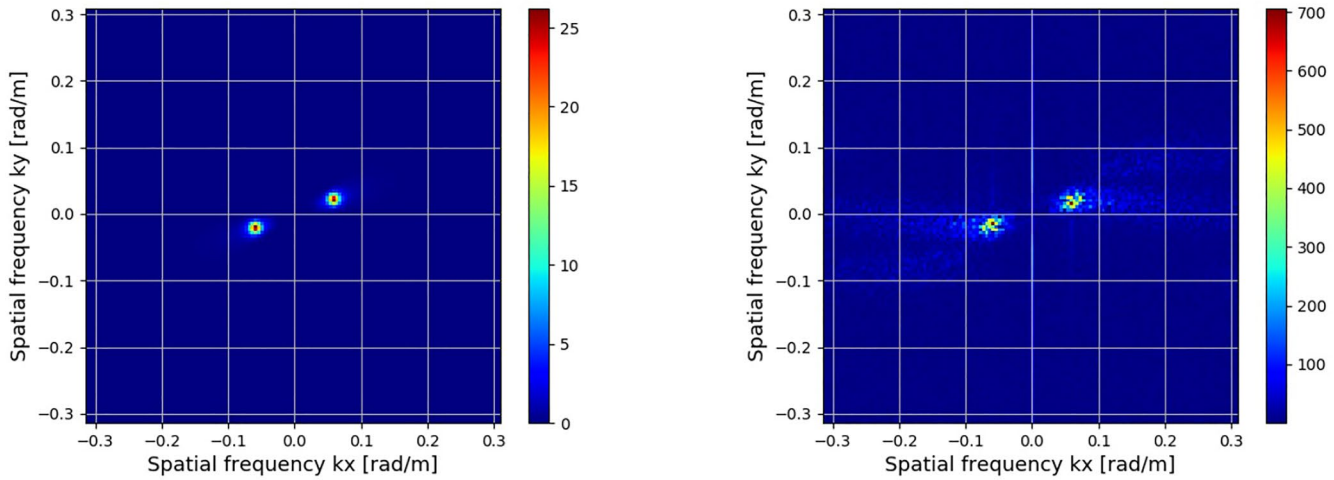

(a) Sampled directional spectrum $\hat{\mathscr{S}}_{2C}$. (b) The spectrum $\mathfrak{F}_D\{\Phi_{ATI}\}$.

Figure A9. The RTW-R18 scenario: the spectra $\hat{\mathscr{S}}_{2C}$ and $\mathfrak{F}_D\{\Phi_{ATI}.\}$.

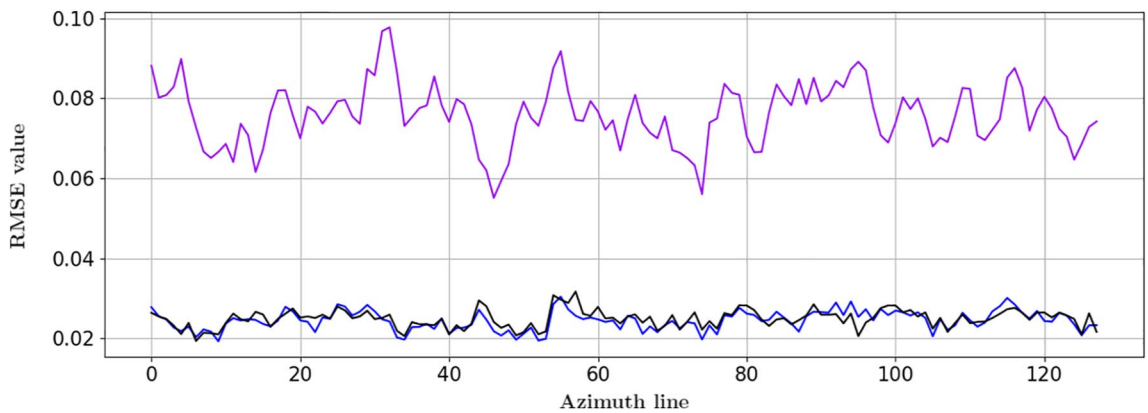

Figure A10. Root Mean Square Error values. Blue: u_r^*–NL, Black: u_r^*–DFM, Violet: u_{ATI}. Each abscissa is a problem.

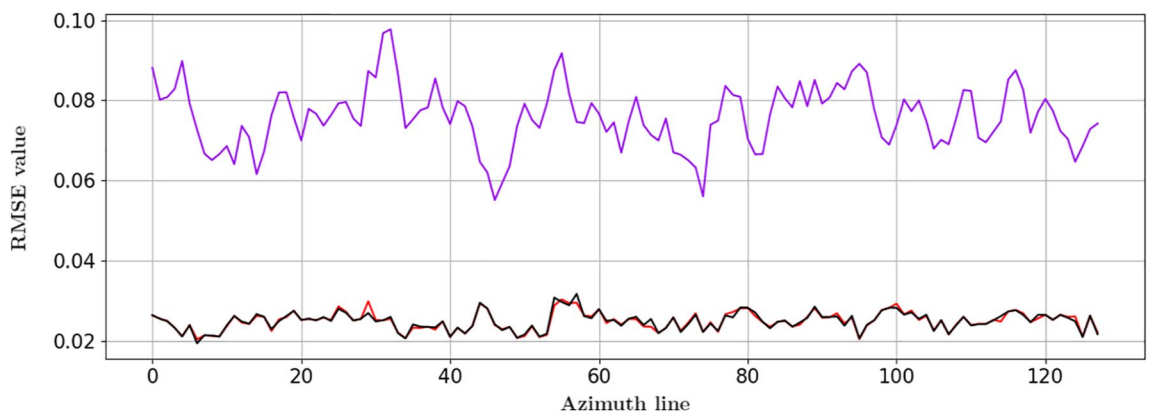

Figure A11. Root Mean Square Error values. Red: u_r^*–FM, Black: u_r^*–DFM, Violet: u_{ATI}. Each abscissa is a problem.

A4. The ATW-R16 Scenario

Table A4, Figure A12, Figure A13, Figure A14

Table A4
The ATW-R16 Scenario: Input and Derived Parameters

Description	Name(s)	Value(s)	Units	Parameter
Wind direction	ϕ_w	$\pi/9$	[rad]	Input
Azimuthal look direction	ϕ_0	$\pi/2$	[rad]	Input
Slant range	R	16×10^3	[m]	Input
Range-to-velocity ratio	R/V	80	[s]	Derived
Variance of surface elevation	$\mathrm{Var}\{z(\mathbf{x}_R, t)\}$	0.020620	[m^2]	Derived
Sample variance of z	s_z^2	0.016873	[m^2]	Derived
Sample significant wave height	$\hat{H}_{m_0}$	0.519591	[m]	Derived
Azimuth SAR resolution	ρ_a	12.77411	[m]	Derived
Vector of radar LOS	v_{LOS}	$\left[0, \frac{\sqrt{2}}{2}, -\frac{\sqrt{2}}{2}\right]^T$	unitary	Derived

Note. First modification of R/V.

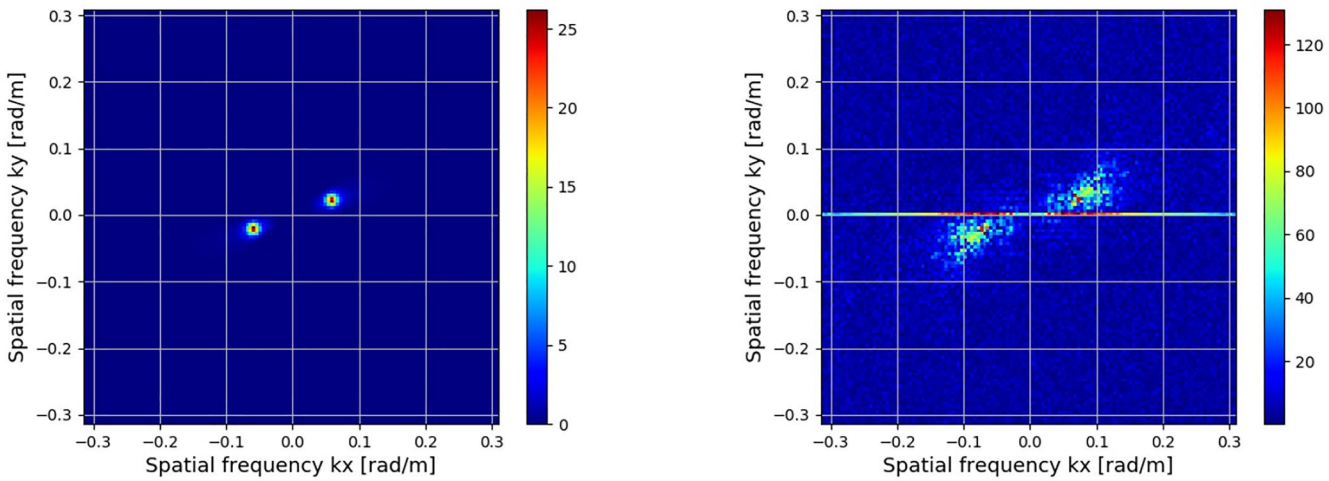

(a) Sampled directional spectrum $\hat{\mathscr{S}}_{2C}$. (b) The spectrum $\mathfrak{F}_D\{\Phi_{ATI}\}$.

Figure A12. The ATW-R16 scenario: the spectra $\hat{\mathscr{S}}_{2C}$ and $\mathfrak{F}_D\{\Phi_{ATI}.\}$.

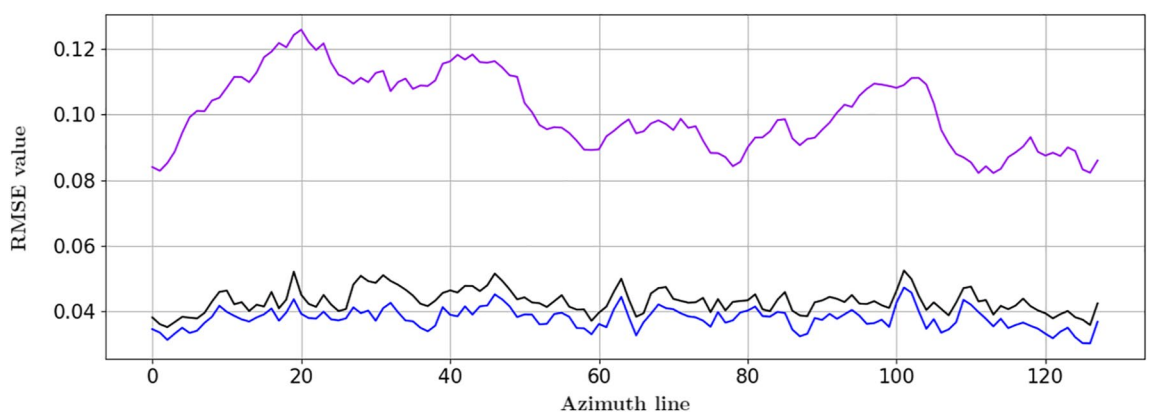

Figure A13. Root Mean Square Error values. Blue: u_r^*–NL, Black: u_r^*–DFM, Violet: u_{ATI}. Each abscissa is a problem.

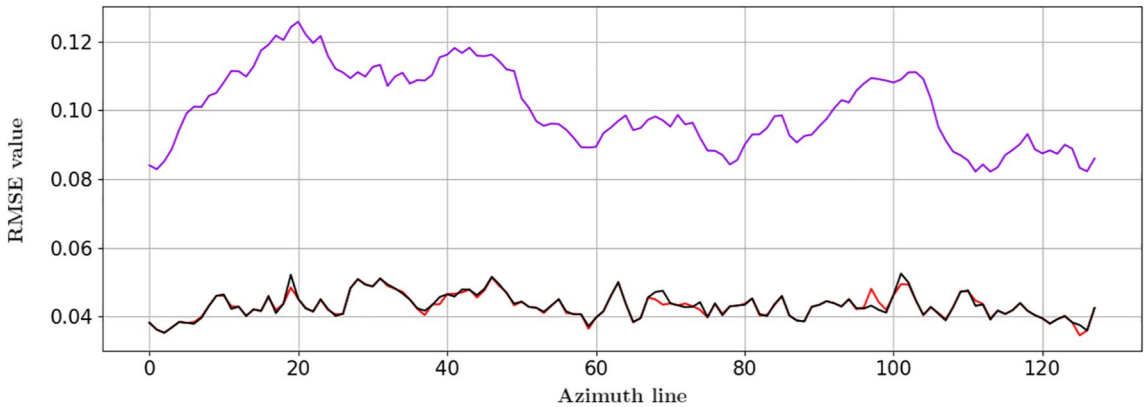

Figure A14. Root Mean Square Error values. Red: u_r^*–FM, Black: u_r^*–DFM, Violet: u_{ATI}. Each abscissa is a problem.

A5. The ATW-R18 Scenario

Table A5, Figure A15, Figure A16, Figure A17

Table A5
The ATW-R18 Scenario: Input and Derived Parameters

Description	Name(s)	Value(s)	Units	Parameter
Wind direction	ϕ_w	$\pi/9$	[rad]	Input
Azimuthal look direction	ϕ_0	$\pi/2$	[rad]	Input
Slant range	R	18×10^3	[m]	Input
Range-to-velocity ratio	R/V	90	[s]	Derived
Variance of surface elevation	$\mathrm{Var}\{z(\mathbf{x}_R, t)\}$	0.020620	[m^2]	Derived
Sample variance of z	s_z^2	0.016873	[m^2]	Derived
Sample significant wave height	$\hat{H}_{m_0}$	0.519591	[m]	Derived
Azimuth SAR resolution	ρ_a	14.37087	[m]	Derived
Vector of radar LOS	v_{LOS}	$\left[0, \frac{\sqrt{2}}{2}, -\frac{\sqrt{2}}{2}\right]^T$	unitary	Derived

Note. Second modification of R/V.

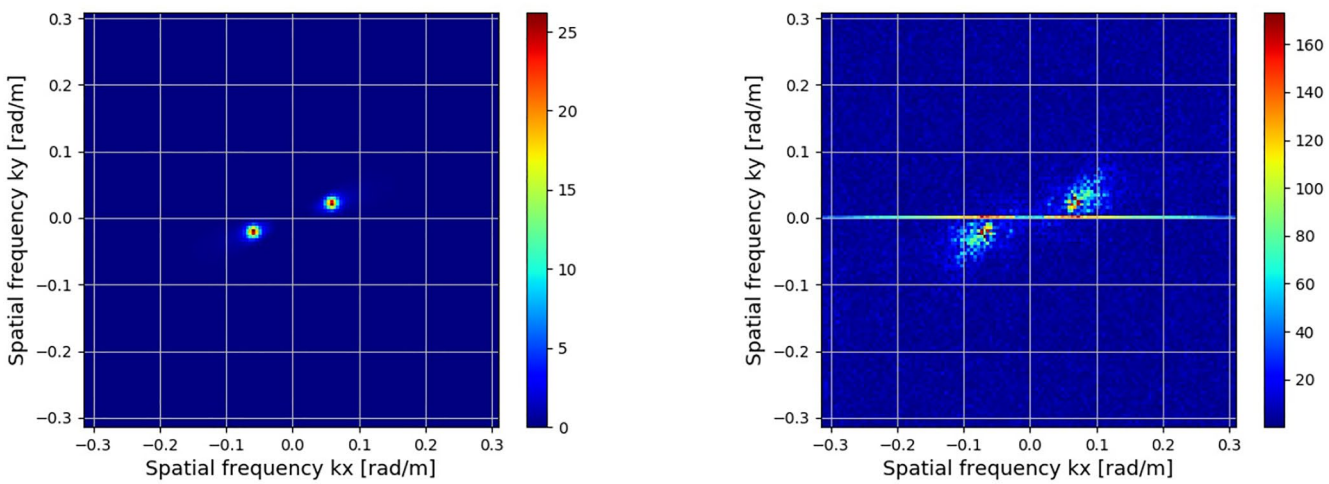

(a) Sampled directional spectrum $\hat{\mathcal{S}}_{2C}$. (b) The spectrum $\mathfrak{F}_D\{\Phi_{ATI}\}$.

Figure A15. The ATW-R18 scenario: the spectra $\hat{\mathcal{S}}_{2C}$ and $\mathfrak{F}_D\{\Phi_{ATI}.\}$.

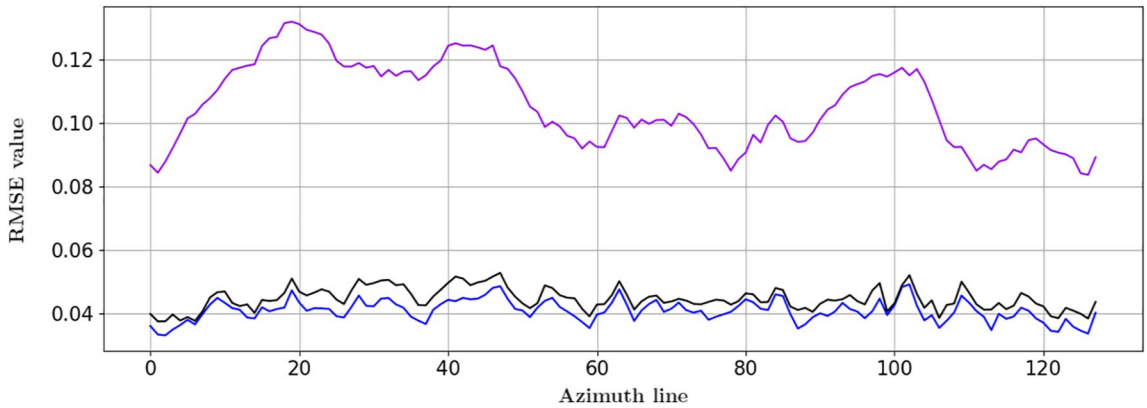

Figure A16. Root Mean Square Error values. Blue: u_r^*–NL, Black: u_r^*–DFM, Violet: u_{ATI}. Each abscissa is a problem.

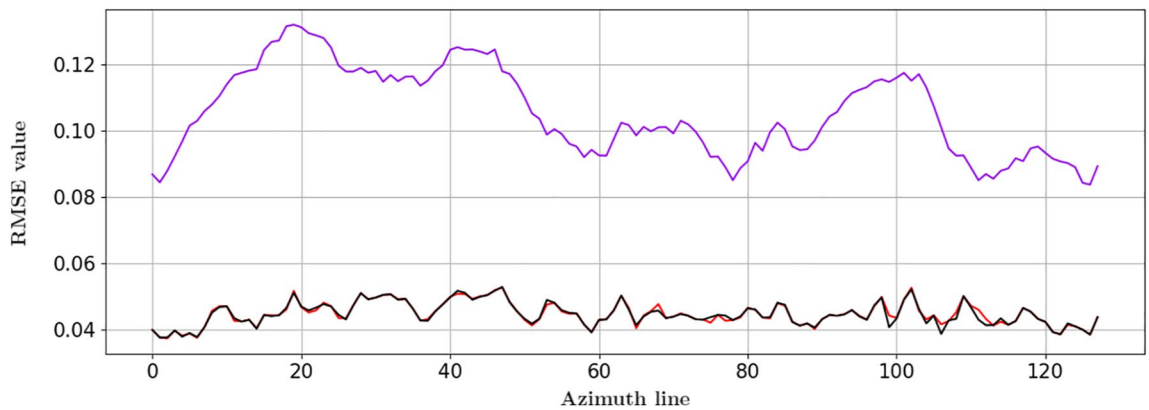

Figure A17. Root Mean Square Error values. Red: u_r^*–FM, Black: u_r^*–DFM, Violet: u_{ATI}. Each abscissa is a problem.

Data Availability Statement

The data sets associated with this paper are available at the Flanders Marine Institute. Data set of Range Travelling Waves: https://doi.org/10.14284/444. Data set of Azimuthally Travelling Waves: https://doi.org/10.14284/446.

Acknowledgments
Research supported in part by Conacyt project A1-S-17634. The authors thank the references for the manuscript has been greatly improved by their thorough reading and very constructive suggestions.

References

Alpers, W. (1983). Monte carlo simulations for studying the relationship between ocean wave and synthetic aperture radar image spectra. *Journal of Geophysical Research*, *88*(C3), 1745–1759. https://doi.org/10.1029/jc088ic03p01745

Alpers, W., & Rufenach, C. (1979). The effect of orbital motions on synthetic aperture radar imagery of ocean waves. *IEEE Transactions on Antennas and Propagation*, *27*(5), 685–690. https://doi.org/10.1109/tap.1979.1142163

Alpers, W. R., Ross, D. B., & Rufenach, C. L. (1981). On the detectability of ocean surface waves by real and synthetic aperture radar. *Journal of Geophysical Research*, *86*(C7), 6481–6498. https://doi.org/10.1029/jc086ic07p06481

Bamler, R., & Hartl, P. (1998). Synthetic aperture radar interferometry. *Inverse Problems*, *14*(4), 1–54. https://doi.org/10.1088/0266-5611/14/4/001

Bao, M., Bruning, C., & Alpers, W. (1997). Simulation of ocean waves imaging by an along-track interferometric synthetic aperture radar. *IEEE Transactions on Geoscience and Remote Sensing*, *35*(3), 618–631. https://doi.org/10.1109/36.581977

Brüning, C., Alpers, W., & Hasselmann, K. (1990). Monte-carlo simulation studies of the nonlinear imaging of a two dimensional surface wave field by a synthetic aperture radar. *International Journal of Remote Sensing*, *11*(10), 1695–1727. https://doi.org/10.1080/01431169008955125

Cheney, E. W. (2001). *Analysis for applied mathematics*. Springer-Verlag.

Estatico, C., Fedeli, A., Pastorino, M., & Randazzo, A. (2015). Buried object detection by means of a lp banach-space inversion procedure. *Radio Science*, *50*(1), 41–51. https://doi.org/10.1002/2014rs005542

Goldstein, R. M., & Zebker, H. A. (1987). Interferometric radar measurement of ocean surface currents. *Nature*, *328*, 707–709. https://doi.org/10.1038/328707a0

Hasselmann, K., & Hasselmann, S. (1991). On the nonlinear mapping of an ocean wave spectrum into a synthetic aperture radar image spectrum and its inversion. *Journal of Geophysical Research*, *96*(C6), 10713–10729. https://doi.org/10.1029/91jc00302

Hasselmann, K., Raney, R. K., Plant, W. J., Alpers, W., Shuchman, R. A., Lyzenga, D. R., & Tucker, M. J. (1985). Theory of synthetic aperture radar ocean imaging: A marsen view. *Journal of Geophysical Research*, *90*(C3), 4659–4686. https://doi.org/10.1029/jc090ic03p04659

Hasselmann, S., Brüning, C., Hasselmann, K., & Heimbach, P. (1996). An improved algorithm for the retrieval of ocean wave spectra from synthetic aperture radar image spectra. *Journal of Geophysical Research*, *101*(C7), 16615–16629. https://doi.org/10.1029/96jc00798

Holthuijsen, L. H. (2007). *Waves in oceanic and coastal waters*. Cambridge University Press.

Hwang, P. A., Toporkov, J. V., Sletten, M. A., & Menk, S. P. (2013). Mapping surface currents and waves with interferometric synthetic aperture radar in coastal waters: Observations of wave breaking in swell-dominant conditions. *Journal of Physical Oceanography*, *43*(3), 563–582. https://doi.org/10.1175/jpo-d-12-0128.1

Mobley, C. D. (2016). *Modeling sea surfaces. A tutorial on fourier transform techniques. version 2.0*. Sequoia Scientific, Inc.

Moiseev, A., Johnsen, H., Johannessen, J. A., Collard, F., & Guitton, G. (2020). On removal of sea state contribution to sentinel-1 doppler shift for retrieving reliable ocean surface current. *Journal of Geophysical Research: Oceans*, *125*(9), e2020JC016288. https://doi.org/10.1029/2020jc016288

Moreira, A., Prats-Iraola, P., Younis, M., Krieger, G., Hajnsek, I., & Papathanassiou, K. P. (2013). A tutorial on synthetic aperture radar. *IEEE Geoscience and Remote Sensing Magazine*, *1*(1), 6–43. https://doi.org/10.1109/mgrs.2013.2248301

Stuart, A. M. (2010). Inverse problems: A Bayesian perspective. *Acta Numerica*, *19*, 451–559. https://doi.org/10.1017/s0962492910000061

Vogel, C. R. (2002). *Computational methods for inverse problems*. Society for Industrial and Applied Mathematics (SIAM).

Yoshida, T. (2016). Numerical research on clear imaging of azimuth-traveling ocean waves in sar images. *Radio Science*, *51*(7), 989–998. https://doi.org/10.1002/2016rs006000

Zuazua, E. (2005). Propagation, observation, and control of waves approximated by finite difference methods. *SIAM Review*, *47*(2), 197–243. https://doi.org/10.1137/s0036144503432862